Supplementary Information

Interface Property-Functionality Interplay: Suppresses Bimolecular Recombination Facilitating Above 18% Efficiency Organic Solar Cells Embracing Simplistic Fabrication

Top Archie Dela Peña, Ruijie Ma,* Zengshan Xing, Qi Wei, Jafar I. Khan, Ryan Michael Young, Yulong Hai, Sheena Anne Garcia, Xinhui Zou, Zijing Jin, Fai Lun Ng, King Lun Yeung, Dayne F. Swearer, Michael R. Wasielewski, Jiannong Wang, Hyojung Cha, He Yan, Kam Sing Wong, Gang Li,* Mingjie Li,* and Jiaying Wu*

Contents

Supplementary Figures and Discussion

Supplementary Tables and Discussion

Supplementary Notes

Supplementary Figures and Discussion

1. Absorption and optical bandgap estimations
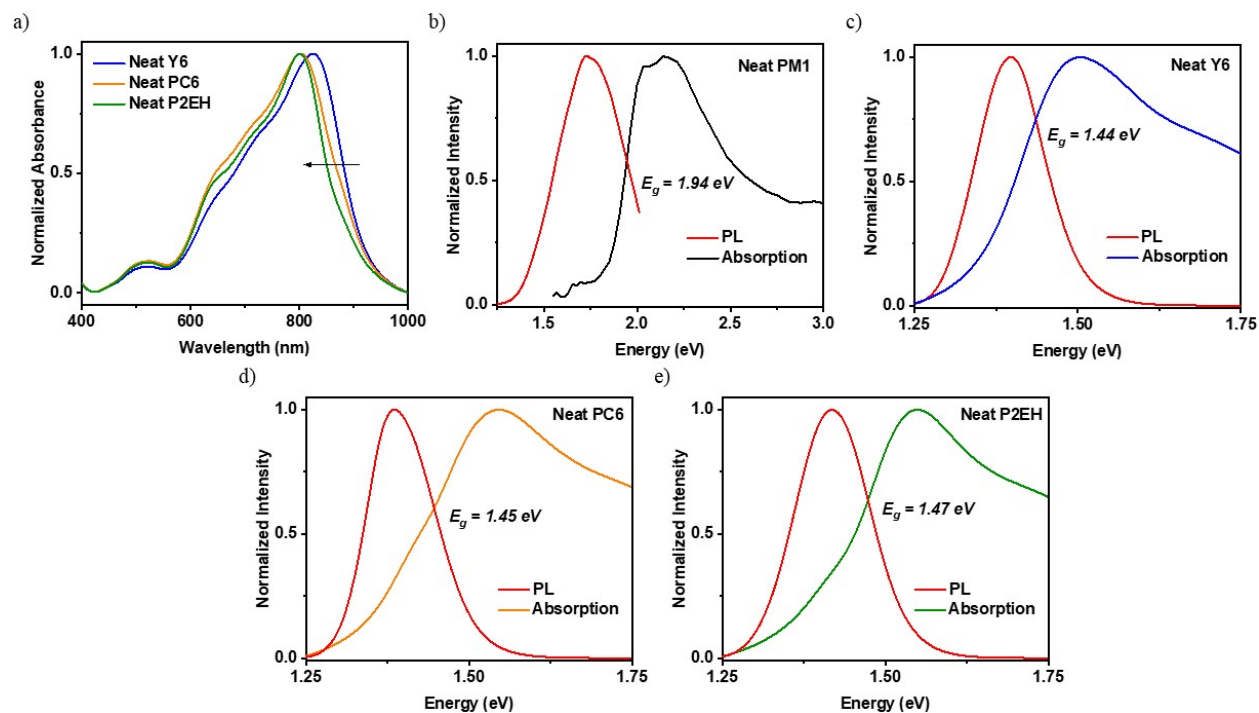
Fig. S1. NFAs absorption (a) and intersection with photoluminescence (PL) to quantify the optical bandgap E_g (b-e).

Discussion: The absorption onsets are consistent with an earlier report suggesting that the bulkier outer side groups present in PC6 and P2EH can reduce aggregations causing absorption hypsochromic shift,[1] justifying their relative values for open circuit voltage (V_{OC}). It must also be noted that such aggregation size does not directly translate to crystallinity.[2] The optical gap is estimated as the absorption and photoluminescence (PL) spectra intersection in the energy (E) scale. The PL spectra are obtained using either 633 nm or 514 nm excitation wavelengths and divided by E^2 before normalization to account for the Jacobian correction.

2. Photovoltaic bandgap
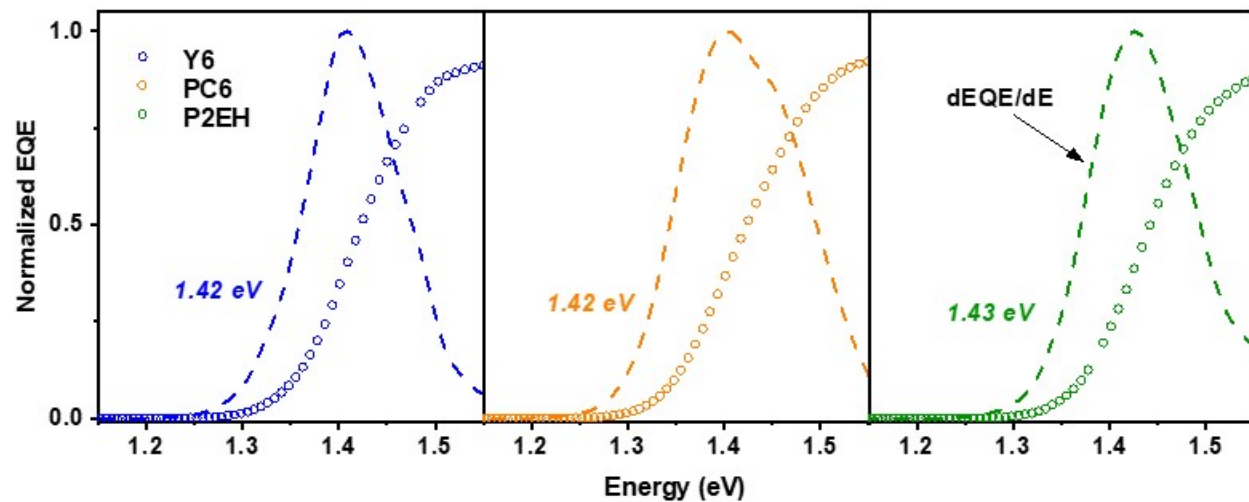
Fig. S2. Low energy tails of EQE spectra. The dashed lines are the differential EQE (*dEQE/dE*) used as probability density to calculate the photovoltaic bandgap of PM1:NFA devices. These are derived from sensitively measured EQE, plotted as open circles.

3. Ultraviolet photoelectron spectroscopy
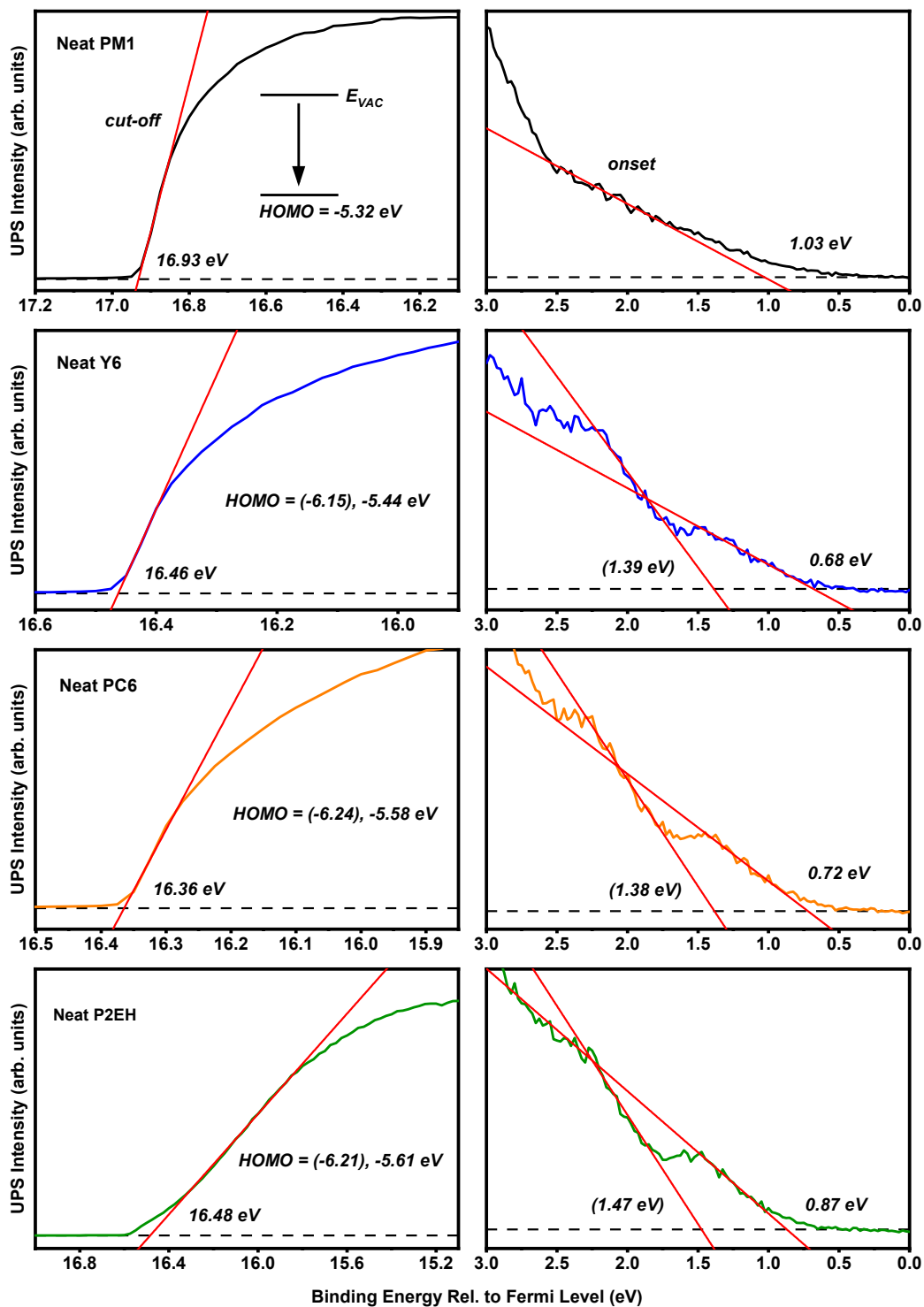
Fig. S3. UPS onset and cut-off regions. The values inside the parenthesis are descriptive of the NFAs more ordered phase. The estimated HOMO energy levels are referenced to vacuum (E_{vac}).

Discussion: The transport energy levels, known as highest occupied molecular orbital (HOMO) and lowest unoccupied molecular orbital (LUMO), are typically identified through both solution-state and solid-state (e.g., thin films). Cyclic voltammetry (CV) is commonly employed for solutions wherein there is absence of order while photoelectron spectroscopy is for thin films in which molecules are capable of displaying more compact packing.

Herein, ultraviolet photoelectron spectroscopy (UPS) is used to determine the HOMO levels (Fig. S3). Upon closer inspection, it is speculative that all the NFAs have two apparent onset regions while only one is recognizable from the donor PM1. When considering the lower energy onset, the estimated HOMO levels are in close agreements with those previously reported for solution state using CV.[3] Conversely, much deeper HOMO levels are obtained from the higher energy onset. The energy level of the polymer PM1 is not significantly influenced by disorder. This behavior is also observed in other high-efficiency polymers such as PM6.[3] For the case of the NFAs, the two apparent onset regions can be associated with the disorder of different phases present. In thin films, neat NFAs can have both aggregate phase (i.e., more compact) and aggregate-aggregate interface (i.e., more randomly oriented). The higher energy onset associates with a more disordered phase owing to good match with CV measurements. Hence, the lower energy onset represents the less disordered phase. To substantiate this assignment, the actual device metrics were taken into consideration. After charge dissociation, polarons from D/A interface will transport through NFA-rich domains and polymer network until extraction/recombination. Consequently, the quasi-Fermi level splitting (*QFLS*) of the free electron and hole polarons will depend on NFA-rich domains LUMO and PM1 HOMO, which can be approximated as the device V_{OC}. As the PM1 HOMO is already extracted from UPS, the NFA-rich domains LUMO can then be estimated. Further, the NFA transport gap ($E_{transport}$) can be defined from the offset of the identified LUMO and UPS HOMO while the optical gap (E_{opt}) is determined from absorption and photoluminescence spectra intersection (Fig. S1). The difference in transport gap and the optical gap is known as the singlet exciton binding energy (E_b), identified herein to be 260 meV for Y6, 340 meV for PC6, and 310 meV for P2EH. Interestingly, these values are consistent with previous studies suggesting around 300 meV for other high efficiency Y-series NFA-based OSCs.[4,5] Furthermore, by adopting the same transport gap to estimate the LUMO for NFA disordered phase, the values obtained also closely approach those reported from disordered solution state using CV.[3] Intuitively, the high energy and low energy onset assignments

reflect the actual device/material properties. It can then be understood that depending on the nature of D/A interface disorder in blends, there will be an upshift in the NFAs transport energy level relative to those within molecular domains. The relevant equations are listed below.

$$LUMO_{NFA} = HOMO_{PM1} + QFLS$$

$$E_{transport} = LUMO - HOMO$$

$$E_b = E_{transport} - E_{opt}$$

As a note, PM1 LUMO is estimated directly from its optical gap as high-efficiency polymer donors are known to have smaller exciton binding energies.[4] Furthermore, these ordered phase transport energy estimations can only provide an overview of the energy landscape as they may convolutes with the solid-state HOMO-1. In fact, earlier studies based on bilayer films have shown that the ionization energies (or equivalently HOMO) from disordered molecular interfaces to purer regions can be up to around 500 - 1000 meV lifted,[6] thereby making the deconvolution with other frontier orbitals of the valance region challenging, more particularly in the actual photoactive layer blend films. Nevertheless, all these are establishing the disorder-induced energy level transition which can also be conceived from other measurements (e.g., solution-state against solid-state energies and charge carrier dynamics).[3] Meanwhile, the exact methodology and experimental approach to explicitly and quantitatively assign the transport energies corresponding to different phases present in a bulk film are still subject to further research and instrumental developments.

4. Photovoltaic performance under 1 Sun illumination
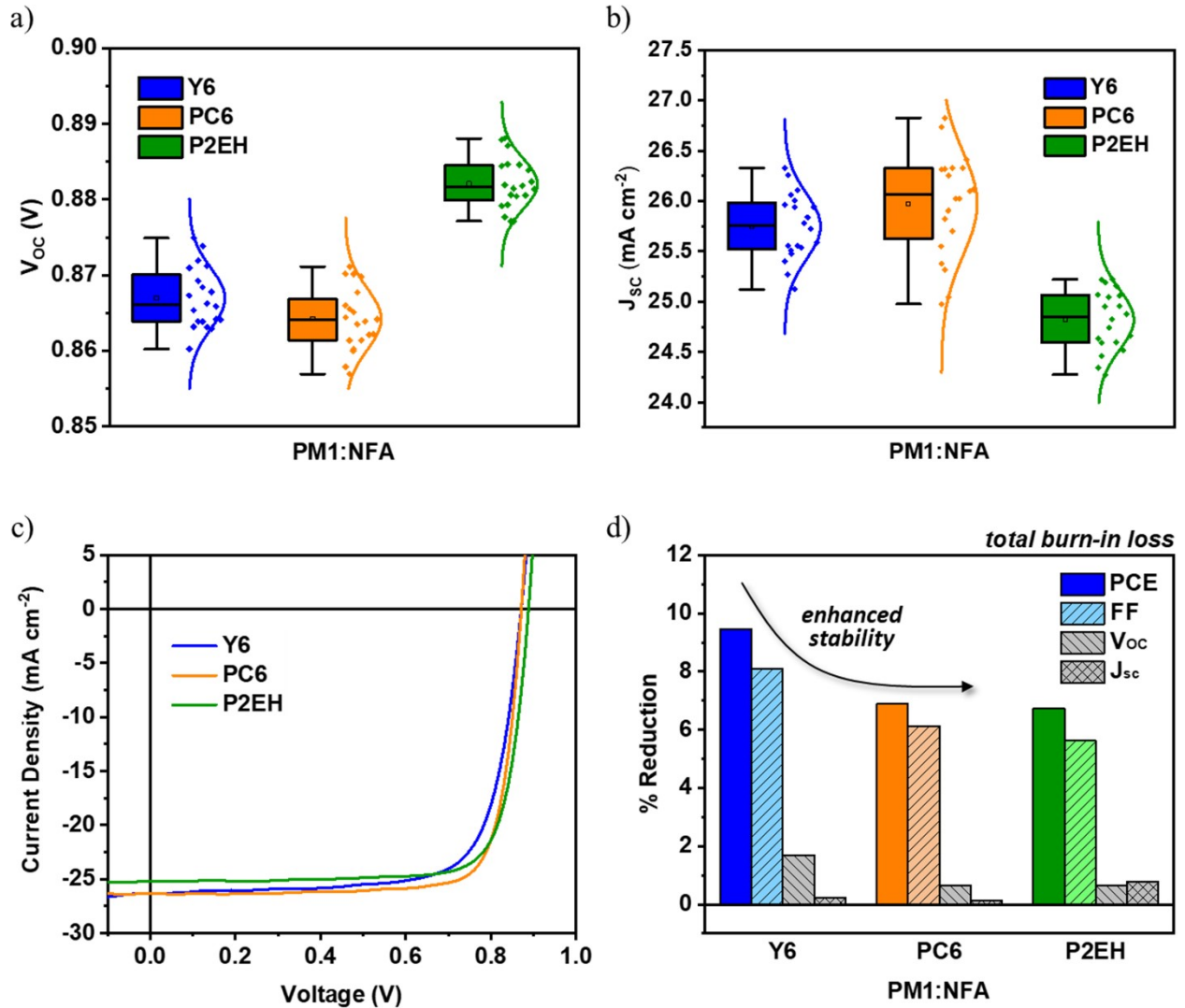
Fig. S4. Device open circuit voltage (a), fill factor (b), current density-voltage curves (c), and EQE (d). These metrics are obtained from bulk heterojunction binary blends of PM1 with the NFA and statistics are based on at least 20 independent working solar cells.

5. Re-organization energy and temperature dependence of CTS EL line shape
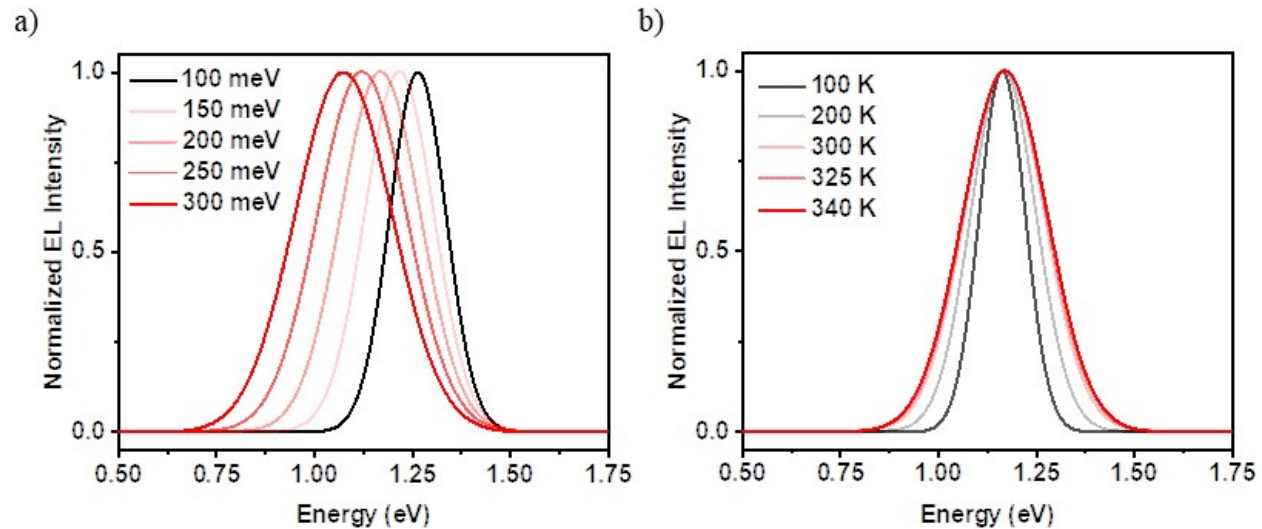
Fig. S5. Simulations of CTS EL spectra based on Marcus formalism with variable re-organization energy (a) and absolute temperature (b). These results are defined using a constant CTS energy of 1.36 eV. Nonetheless, this constant will not have any influence on the relevant interpretations done.

6. Electroabsorption and DFT calculations
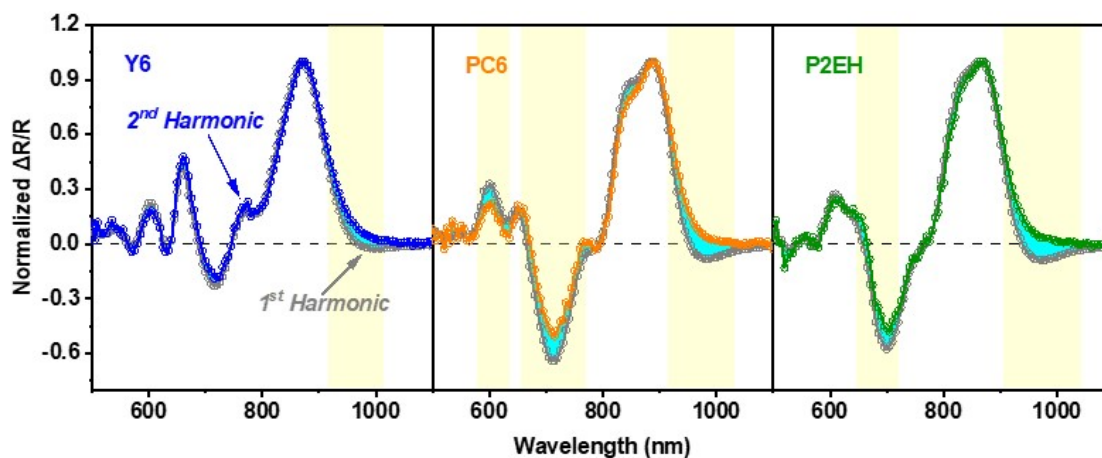
Fig. S6-1. PM1:NFA device electroabsorption spectra based on reflectance geometry measurements.
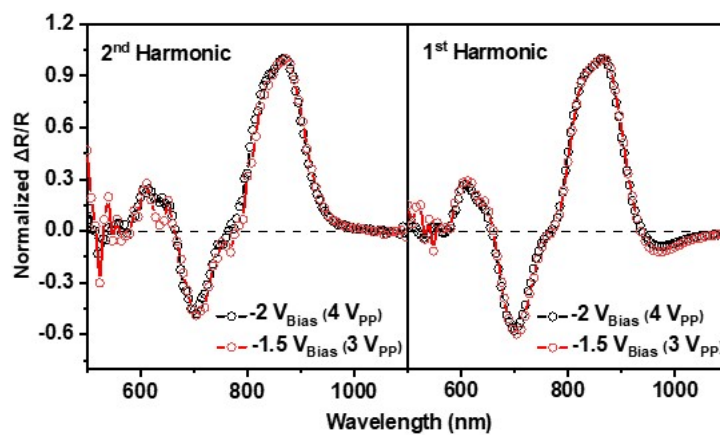
Fig. S6-2. Electro absorption at a different applied bias (V_{Bias}) and amplitude voltage (V_{PP}). The device based on PM1:Y6 is used as the representative sample.
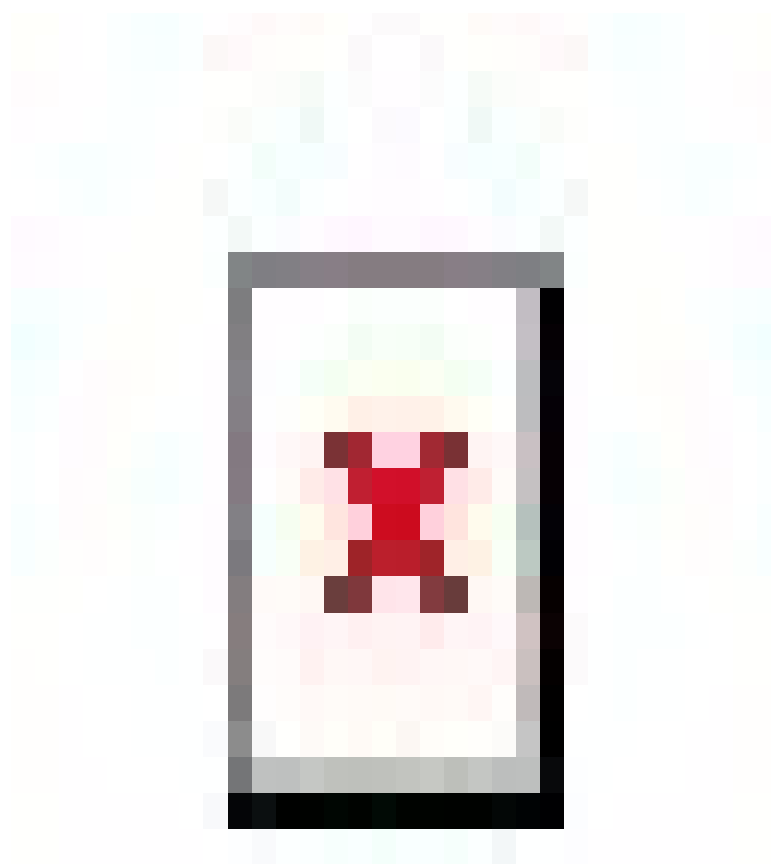
Fig. S6-3. Geometry optimization molecular structure with full side chain, dihedral angles between the backbone and side chain, and dipole moment components in x, y, and z directions: Y6 (a); PC6 (b); and P2EH (c).

Discussion: Unlike Y6, the asymmetry in the Y and Z directions for PC6 and P2EH is exacerbated by the distortion caused by the benzene present on their outer side chains, resulting in a much larger dipole moment in the respective directions of the molecule. P2EH has a broader outer side chain compared to PC6, resulting in a relatively larger dipole moment in the Y direction.

7. NFAs absorption spectra after burn-in
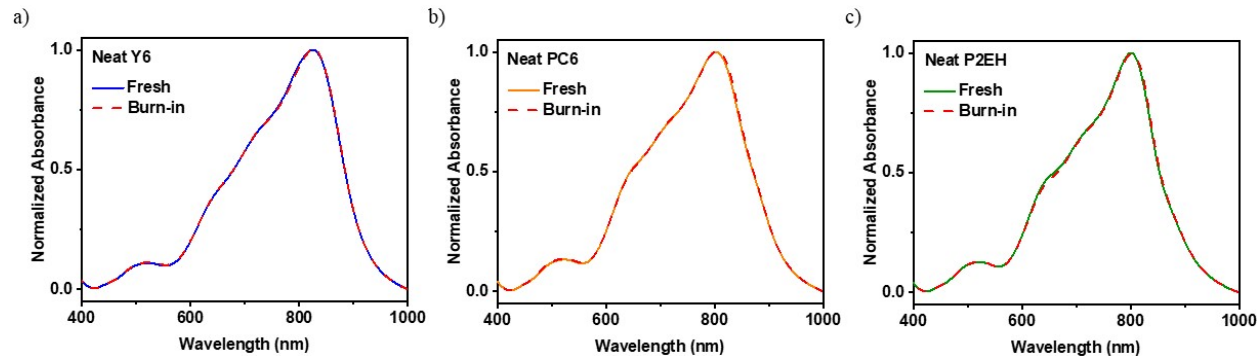
Fig. S7. Absorption spectra of neat acceptors thin film after burn-in degradation. The spectra are normalized to the maximum of fresh samples.

Discussion: No significant changes are observable in the absorption intensity and linewidth for NFAs neat films upon burn-in degradation. Hence, the crystallinity of NFA-rich domains in blends must also be stable under such conditions.

8. Urbach energy after burn-in
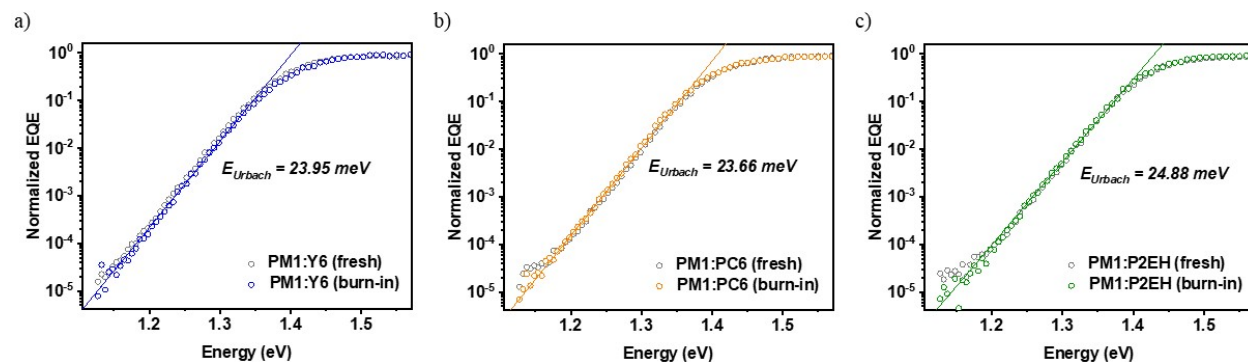
Fig. S8. Urbach energies fitted from the low-energy tail of sensitively measured EQE (open circles).

9. Blends absorption and photoluminescence spectra after burn-in
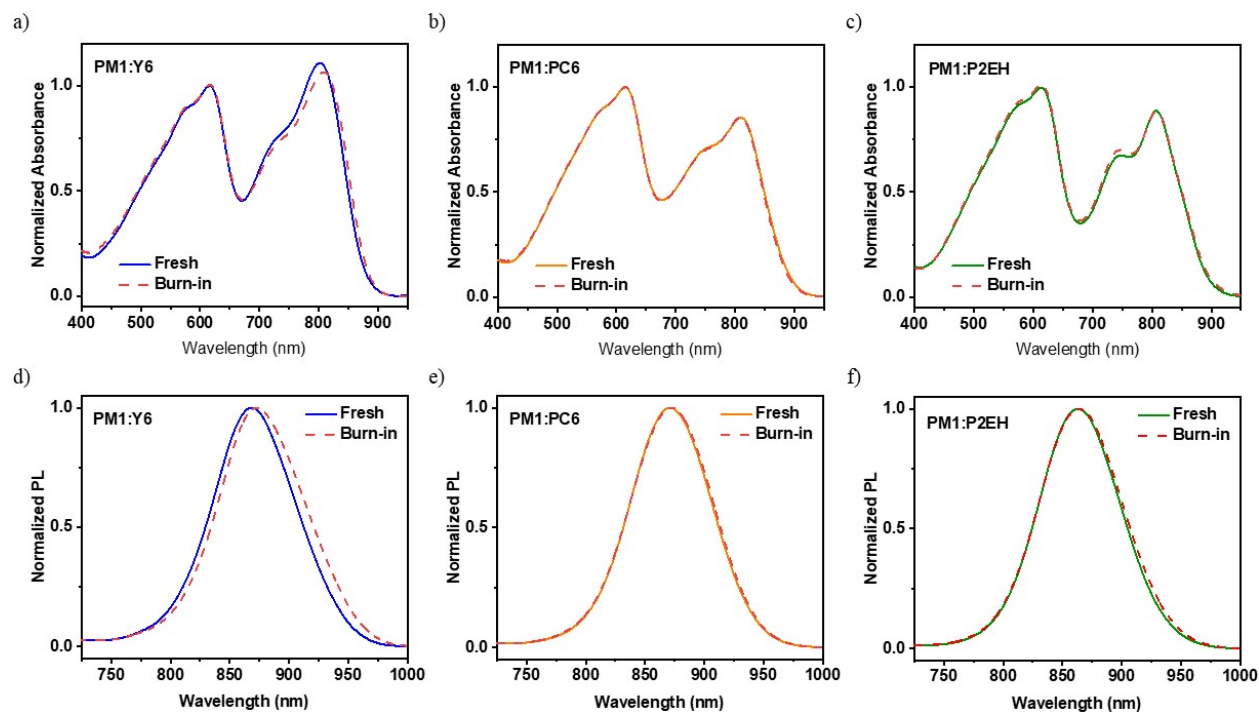
Fig. S9. Blend thin films absorption (a-c) and PL (d-f) spectra after burn-in degradation. The absorbance is normalized relative to the donor peak from fresh samples while the PL is normalized to maximum. The PL is taken using 633 nm excitation wavelength.

Discussion: The PM1:Y6 blend exhibits a drop and redshift in the acceptor absorption range upon burn-in. Because the neat NFAs absorption is previously shown to be stable under the burn-in degradation conditions and their self-assemblies sustain, the observed redshift from the PM1:Y6 blend must then be influenced by the changes in D/A interfaces leading to the formation of smaller crystalline domains.

By turning into the PL spectra wherein the contribution from D/A interfaces are more pronounced, it can also be observed that PM1:Y6 exhibits a significant redshift. From the electroluminescence measurements (EL) in Fig. S11, the CTS energy increases for the burn-in Y6 blend which approach the singlet energy. Hence, the singlet emission will be more visible which peaks at lower wavelength and leads to the apparent redshift in PL. Both PC6 and P2EH-based blends are also sought to have a decent interface and nanomorphology changes but are less sensitive to PL and

absorbance. Hence, EL was further taken advantage of to understand the D/A interfaces by probing emissions directly from such interfaces.

10. Morphology and charge mobility upon burn-in
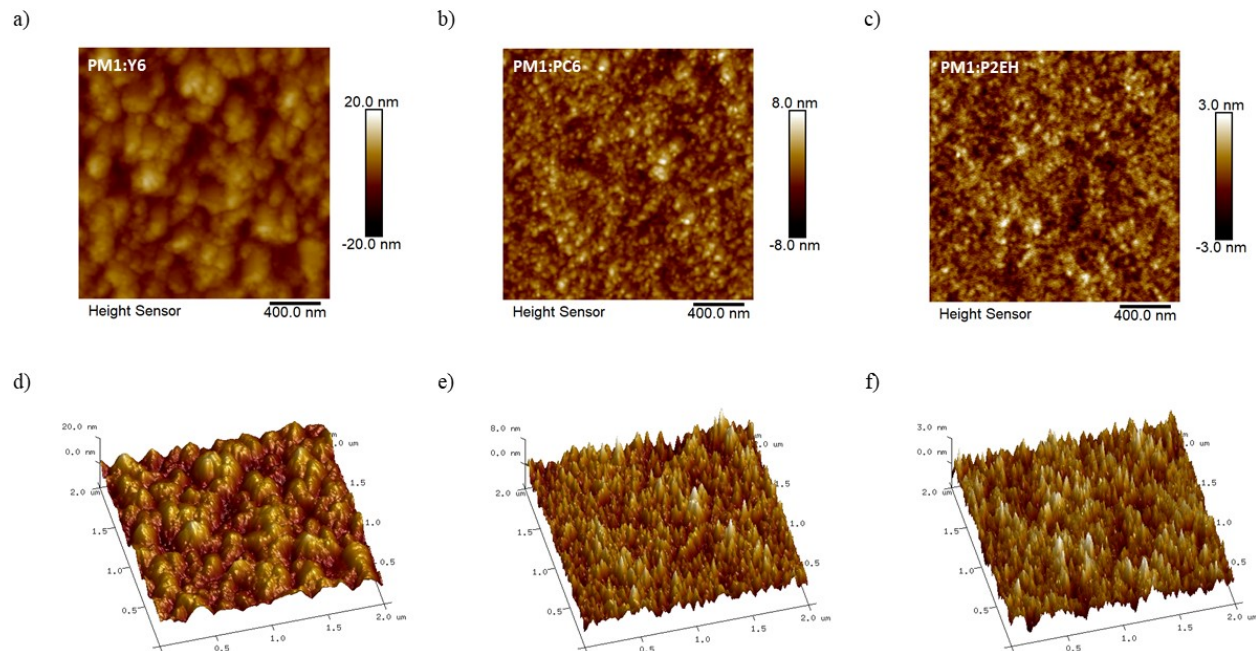
Fig. S10-1. AFM height images of PM1:NFA blends after burn-in.
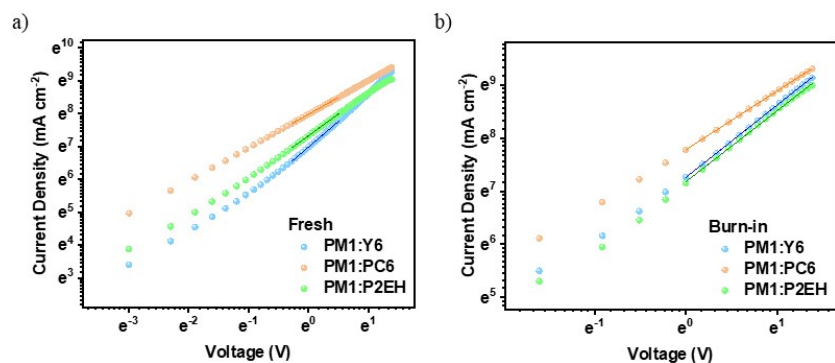
Fig. S10-2. SCLC electron only charge carrier mobilities. The extracted mobilities in 10^{-4} cm^2 V^{-1} s^{-1} are as follows: Y6 (3.67), PC6 (9.98), P2EH (4.96) for fresh and Y6 (4.71), PC6 (8.01), P2EH (4.4) for burn-in. The relative changes upon burn-in reflect their nanomorphology evolution wherein more interconnected networks and smaller domains are expected to impose higher mobilities.

11. Electroluminescence CTS fittings after burn-in
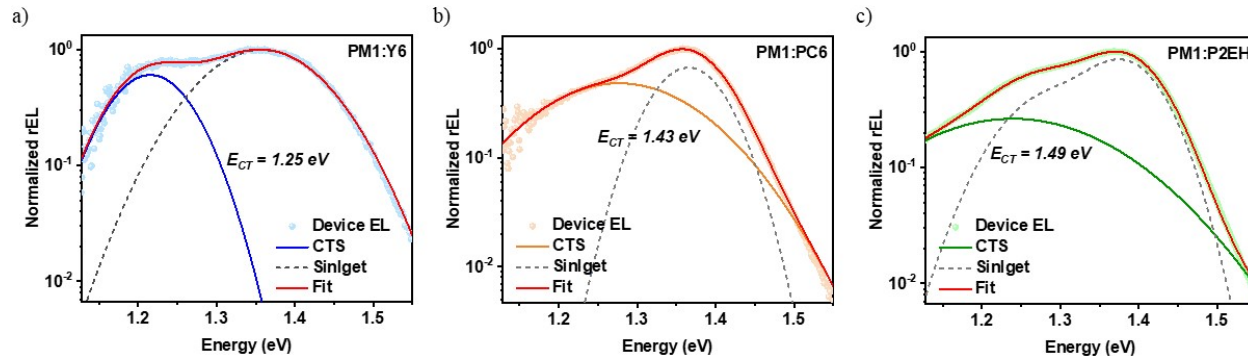
Fig. S11. Fitting curves of the electroluminescence and the identified CTS energy based on the Marcus theory of electron transfer.

12. EQE tail reconstruction
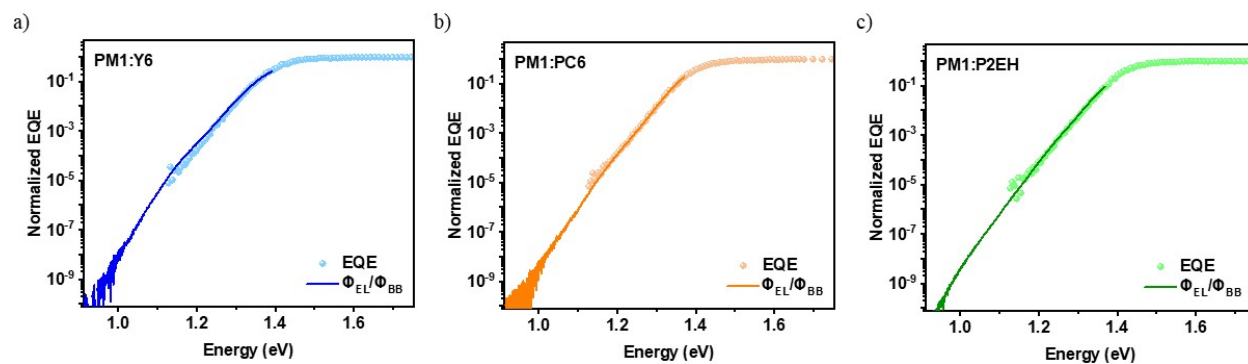
Fig. S12. Reconstruction of sensitively measured EQE tail from blackbody corrected EL (Φ_{EL}/Φ_{BB}) for the energy losses quantification. A more detailed description of the calculation procedure is already provided elsewhere.[7]

13. FTIR spectra
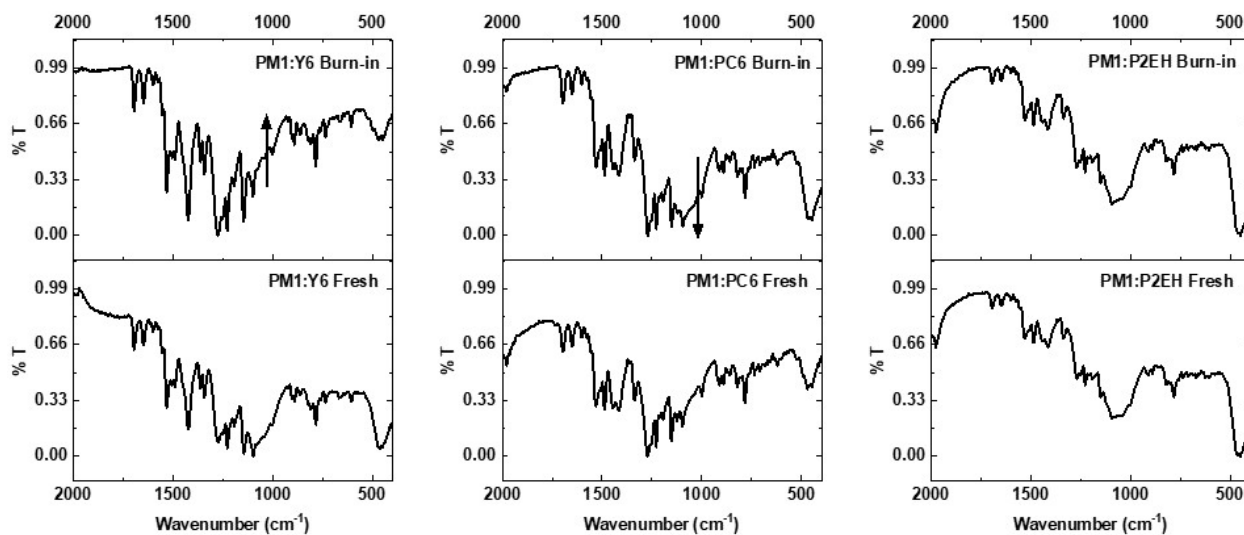
Fig. S13. FTIR spectra from fresh and burn-in degraded films.

14. Transient absorption spectral features assignment (VIS detection range)
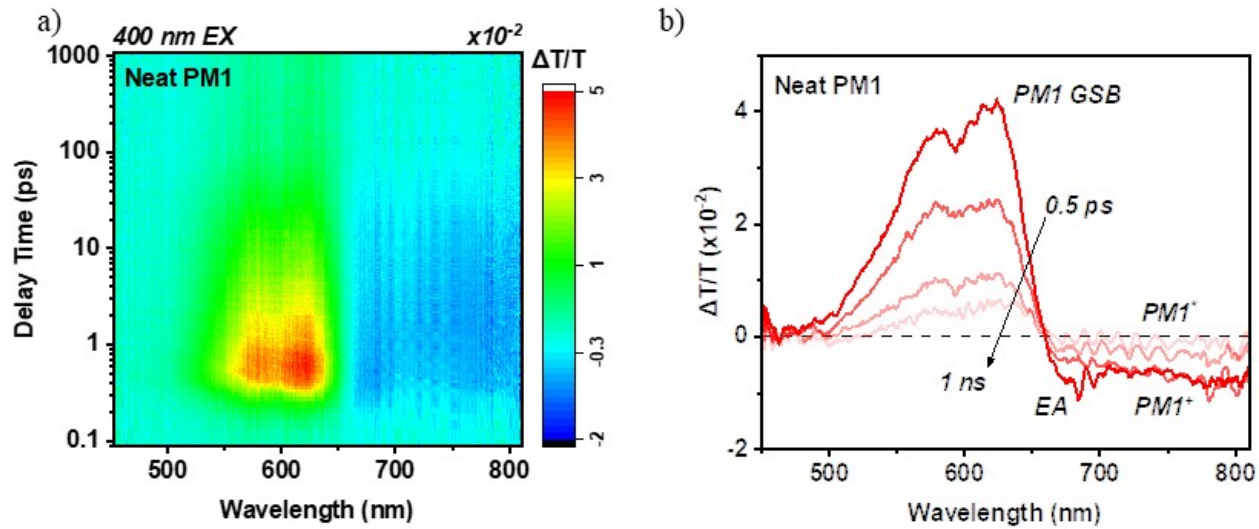
Fig. S14-1. 2D contour plot of neat PM1 thin film transient absorption at 400 nm excitation wavelength (a) and the corresponding spectral line cuts at various delay time (b).
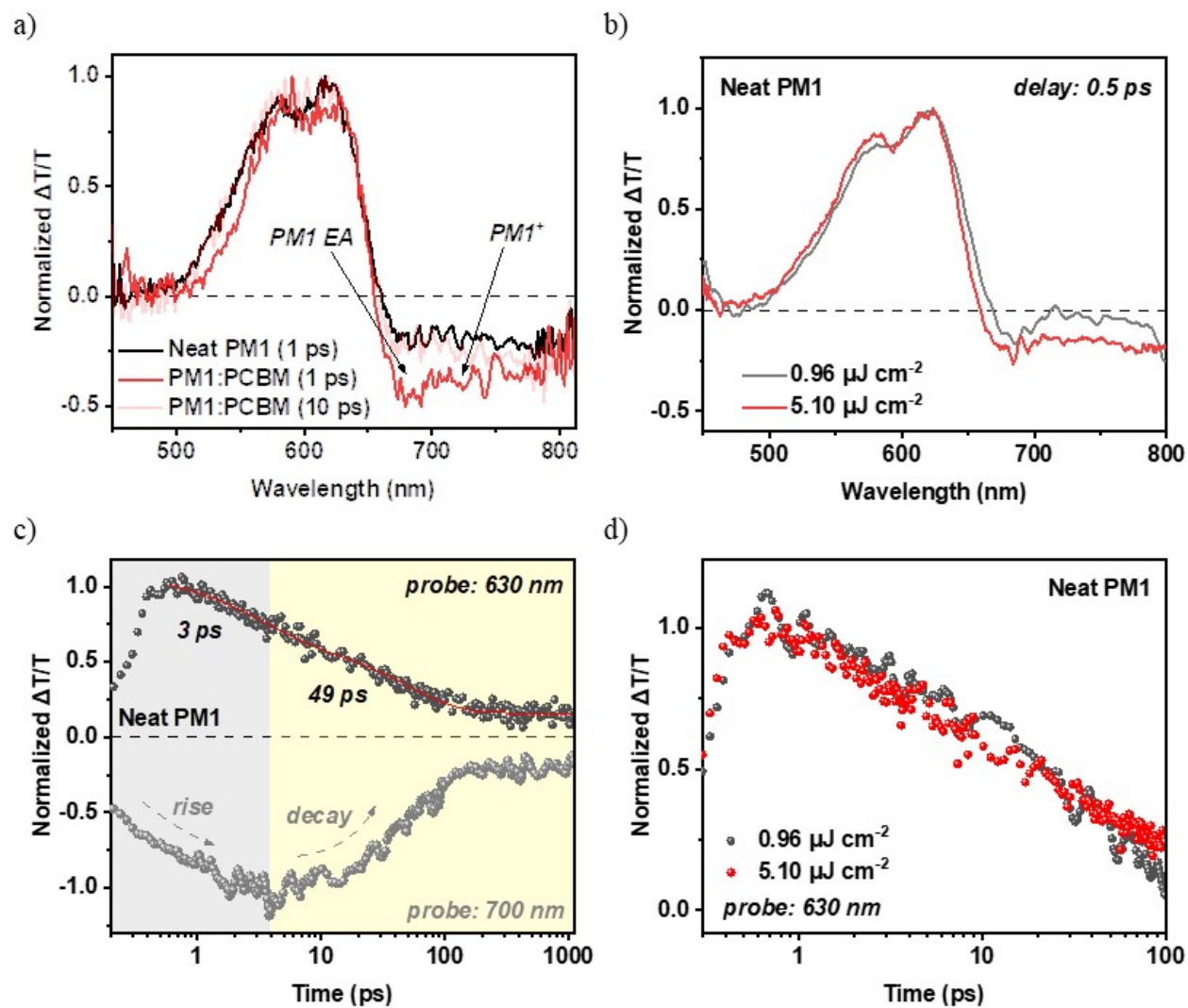
Fig. S14-2. Transient absorption spectral line cuts at different delay time for neat PM1 and PM1:PCBM blend (a), fluence-dependence of neat PM1 spectra after 0.5 ps delay time (b), decay kinetics probed at 630 nm and 700 nm (c), and fluence-dependence of the 630 nm decay. All were taken at 400 nm excitation wavelength.
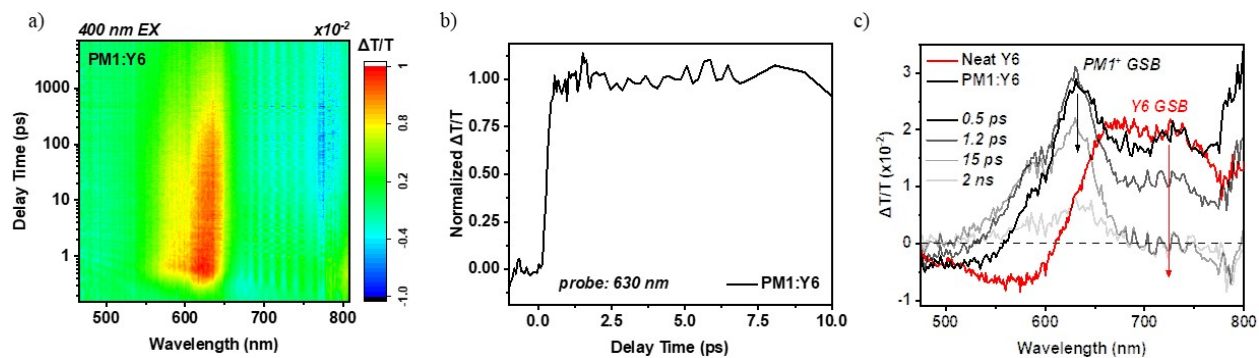
Fig. S14-3. Transient absorption of PM1:Y6 at 400 nm excitation (a), its 630 nm GSB early time kinetics (b), and comparison of neat Y6 with PM1:Y6 visible range spectral line cuts at various delay time upon 800 nm excitation (c).

15. Transient absorption spectral features assignment (NIR detection range)
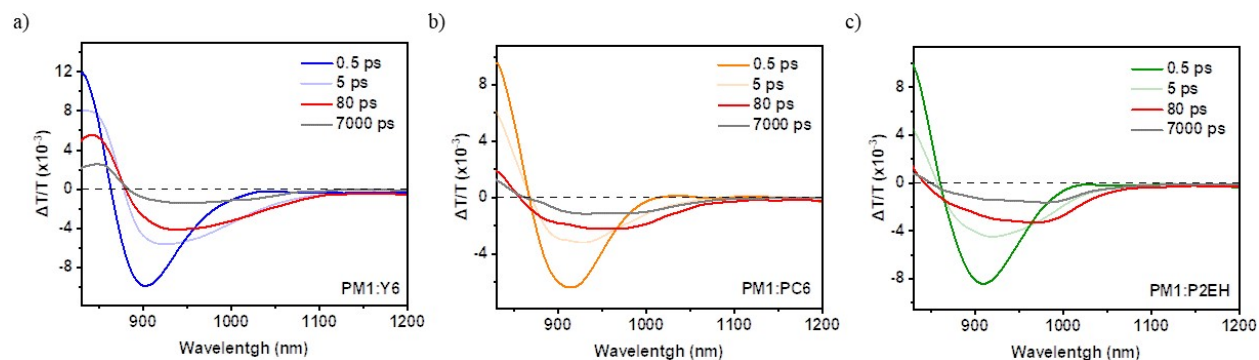
Fig. S15-1. Transient absorption spectral line cuts of PM1:NFA blends at various delay time. Data are obtained using 800 nm excitation.
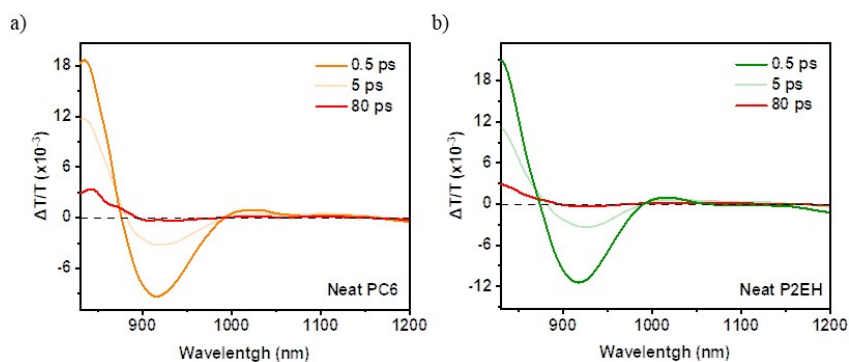
Fig. S15-2. Transient absorption spectral line cuts of neat NFA films at various delay time. Data are obtained using 800 nm excitation. The pure Y6 is already widely reported, which displays similar features as with pure PC6 and P2EH thin films.[3]
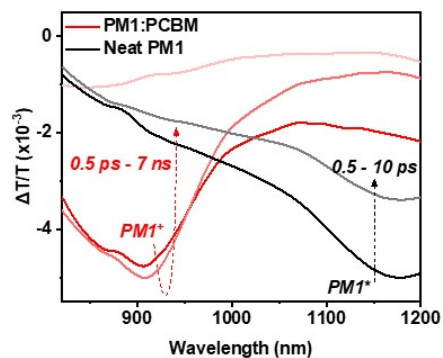
Fig. S15-3. PIA features from transient absorption spectral line cuts of PM1:PCBM and neat PM1 films at various delay time. PM1* is the PM1 singlet excitons while PM1+ is the PM1 hole polarons. Data are obtained using 400 nm excitation. Similar assignments from a related polymer donor PM6 have previously been done.[3]

16. Charge transfer dynamics
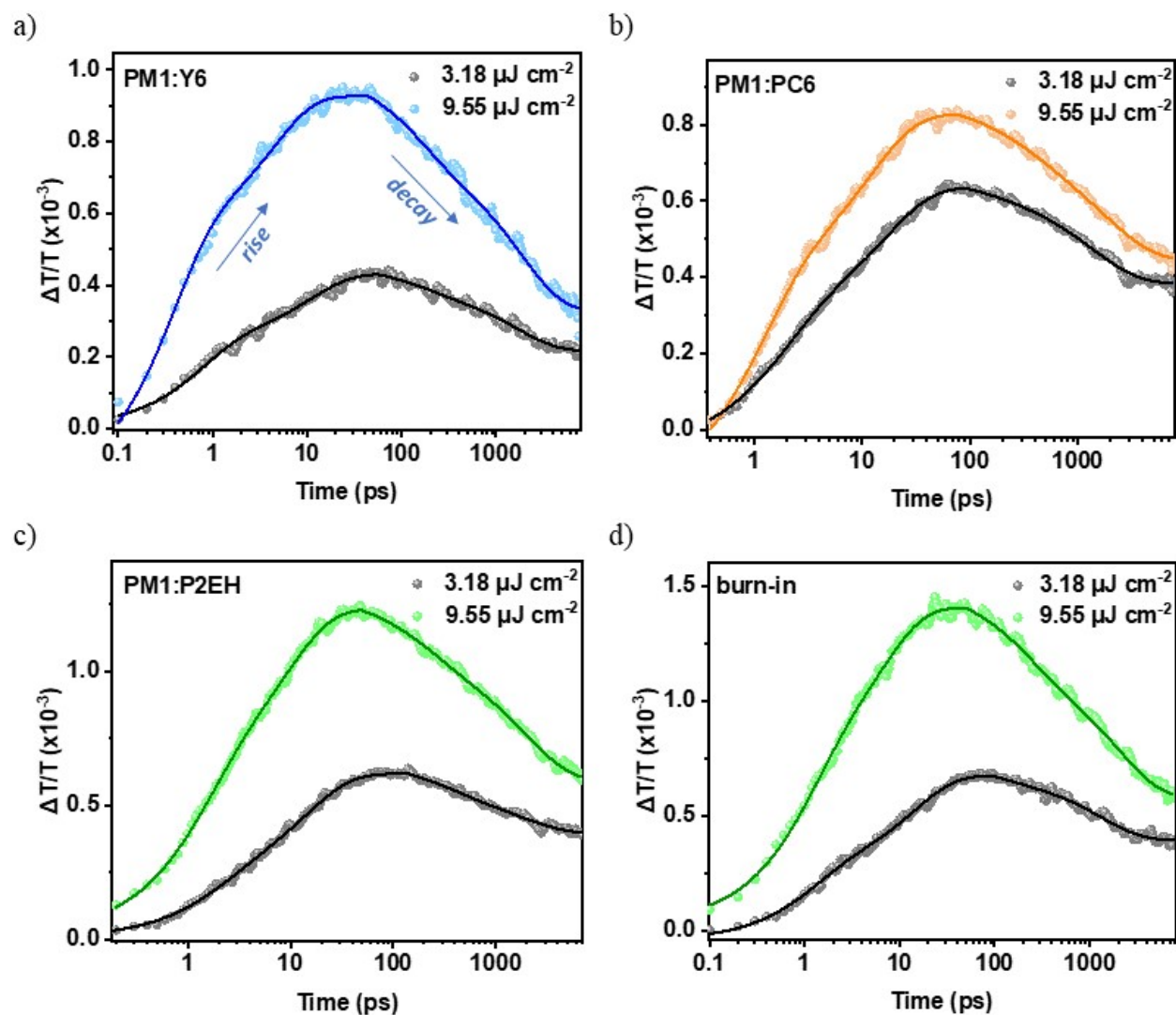
Fig. S16. Rise and decay of NFA electron polarons PIA after selective acceptor excitation (circles). Both the rise and decay are simultaneously fitted using the sum of exponentials and the fitting curves are shown as solid lines.

Discussion: There are different ways to understand the charge transfer dynamics depending on individual cases, herein the rise of NFA^- PIA after selective acceptor excitation is used. As previously shown,[3] the emergence of NFA^- PIA matches the hole transfer kinetics as the exciton dissociation upon hole transfer will generate both hole and electron polarons simultaneously. The changes in NFA singlet GSB can be both from charge transfer and recombination while the rise of

PM1$^+$ GSB is partially convoluted with the decay of NFA singlet GSB and PIA. Hence NFA$^-$ PIA is sought to provide a better overview of the charge transfer dynamics. Nevertheless, it is also shown in the manuscript that the same relative kinetics can be inferred regardless of probing the rise of PM1$^+$ or the NFA$^-$ features upon exciton dissociation.

The charge transfer and dissociation are found to display two components. The faster component can be attributed to excited states formed at the D/A interface and therefore can undergo immediate charge transfer. Consequently, this time constant reflects the upfront charge transfer which can be influenced by several factors such as energy offsets, interface energy, electrostatic effects, energy cascade, and etc. On the other hand, the longer component can be understood as the diffusion-limited charge transfer. In other words, this corresponds to the excited states formed decently away from the D/A interface, requiring exciton diffusion prior to dissociation. Thus, the corresponding time constant substantially depends on the diffusion process. Nevertheless, all the systems considered herein display high EQE (> 80 %), implying highly efficient exciton dissociation. The dissociation rates for Y6 blends are significantly faster than PC6 and P2EH blends regardless of excitation fluence (< 10 μJ cm^{-2}). Further, the burn-in P2EH blend also display faster rates.

17. Mott Schottky Plots
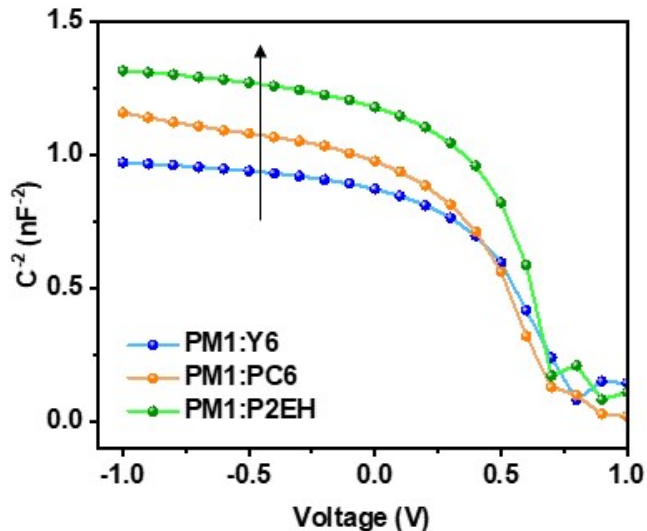
Fig. S17. Mott-Schottky (MS) plots taken under dark and at 1 kHz for PM1:NFA devices where C is the device capacitance. As discussed in earlier works,[7] the upshifted MS curve in the inverse biased region is indicative of higher energy requirement for singlet exciton dissociation which is also reflective of the uphill energy landscape from purer domains to more disordered D/A interfaces. Consistently, P2EH blends with the highest λ_{RO} display the most upshifted MS curve.

18. Hole and electron polaron recombination dynamics
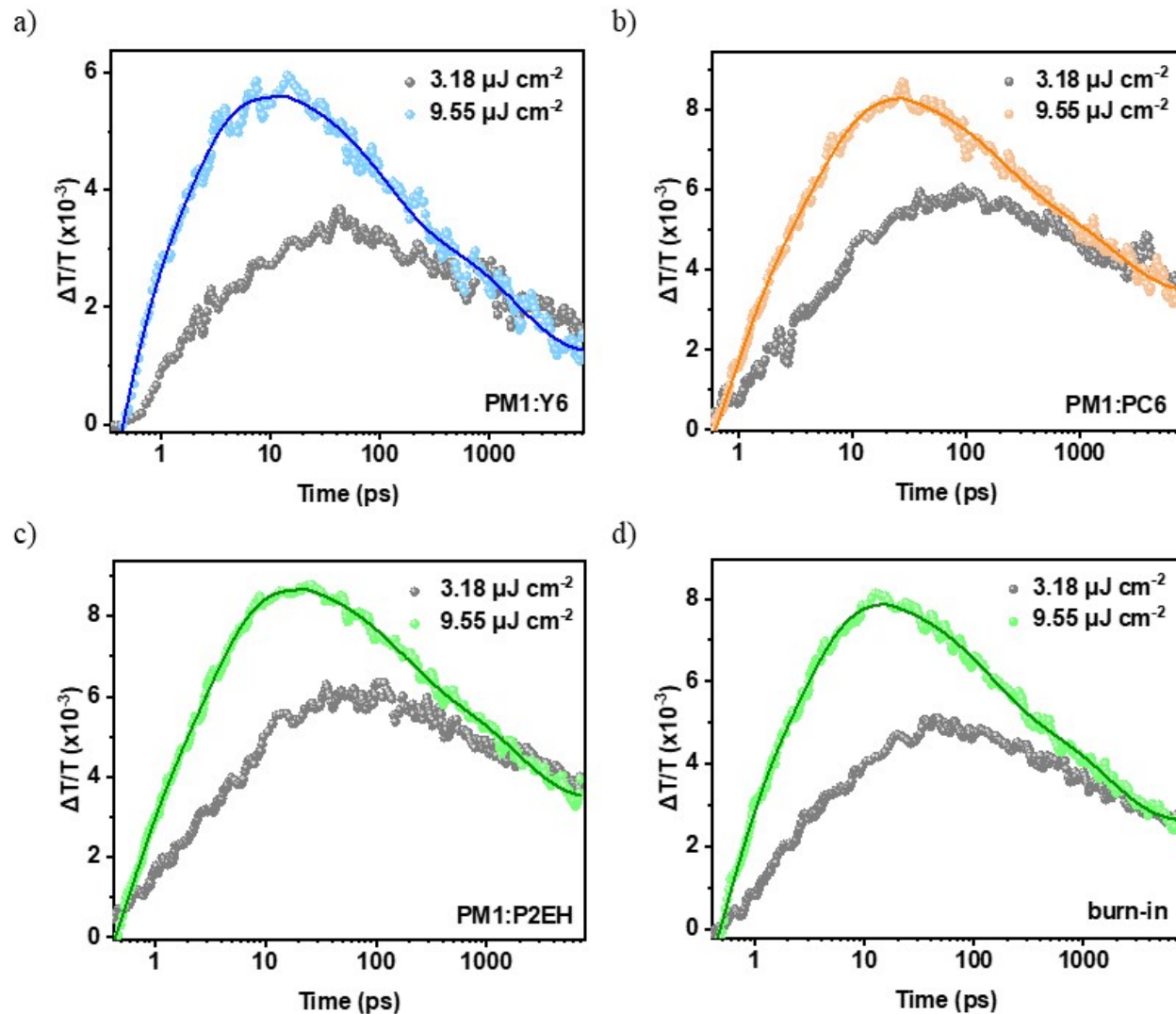
Fig. S18-1. Decay of PM1 hole polarons (PM1$^+$) GSB after selective acceptor excitation (circles) fitted with the sum of exponentials shown as solid lines.

Discussion: After exciton dissociation, the species present will be dominantly hole (PM1$^+$) and electron (NFA$^-$) polarons which are much longer lived compared to most of the singlet exciton population with intrinsic lifetimes identified herein to be < 50 ps (Fig. S. 19). The features with decay extending up to 7000 ps are then dominated by long-lived polarons. Hence, the NFA$^-$ PIA decay (shown in Fig. S16) can be used for the electron polaron recombination while the PM1$^+$ GSB decay is for the hole polaron recombination. Further, the quantified recombination rates are

based on 9.55 µJ cm^{-2} excitation fluence owing to the limit of our measurement delay stage (i.e., maximum of around 7 ns) and to offer fitting values with reasonable error margins. Nevertheless, the same relative decay kinetics can be inferred from lower fluence although they are much slower, as demonstrated in Fig. S18-2.
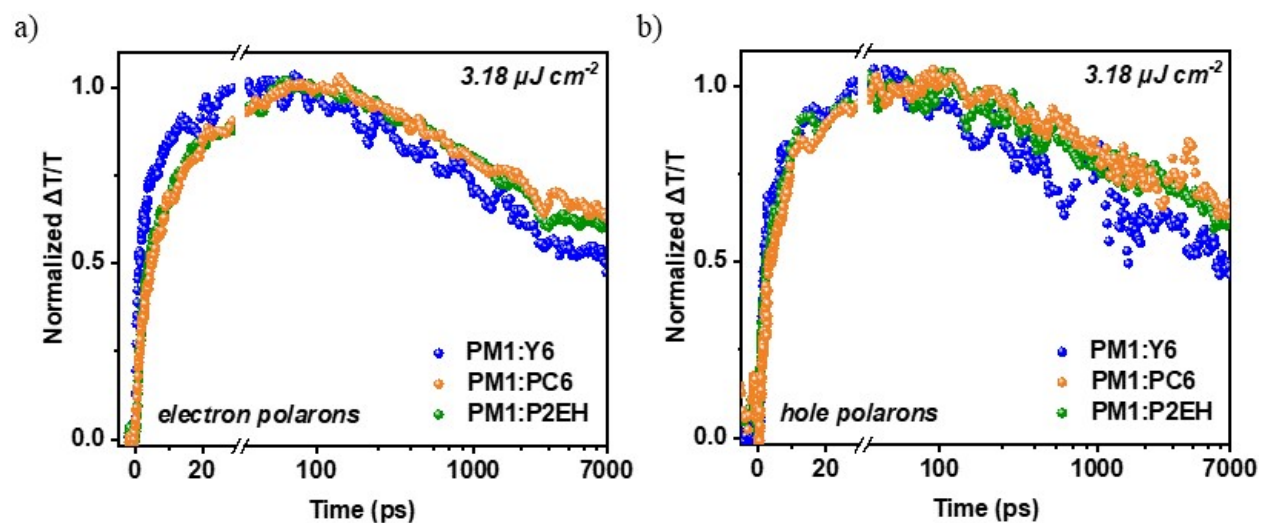
Fig. S18-2. NFA electron polarons and donor hole polarons dissociation and recombination dynamics at lower excitation fluence.

19. NFAs singlet excitons lifetime
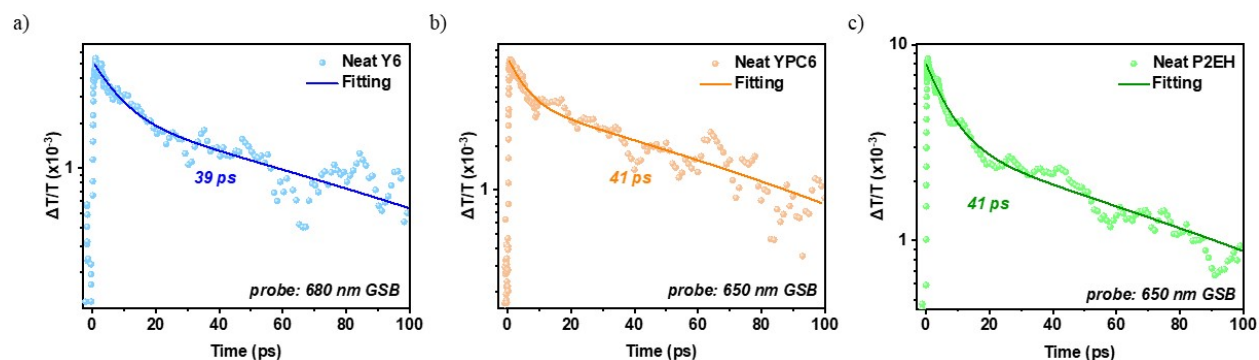
Fig. S19. Decay of NFAs singlet excitons GSB (circles) from neat films at 3.18 μJ cm^{-2} excitation fluence with the corresponding sum of exponentials fitting (solid lines).

20. Framework towards OSCs commercial advancements
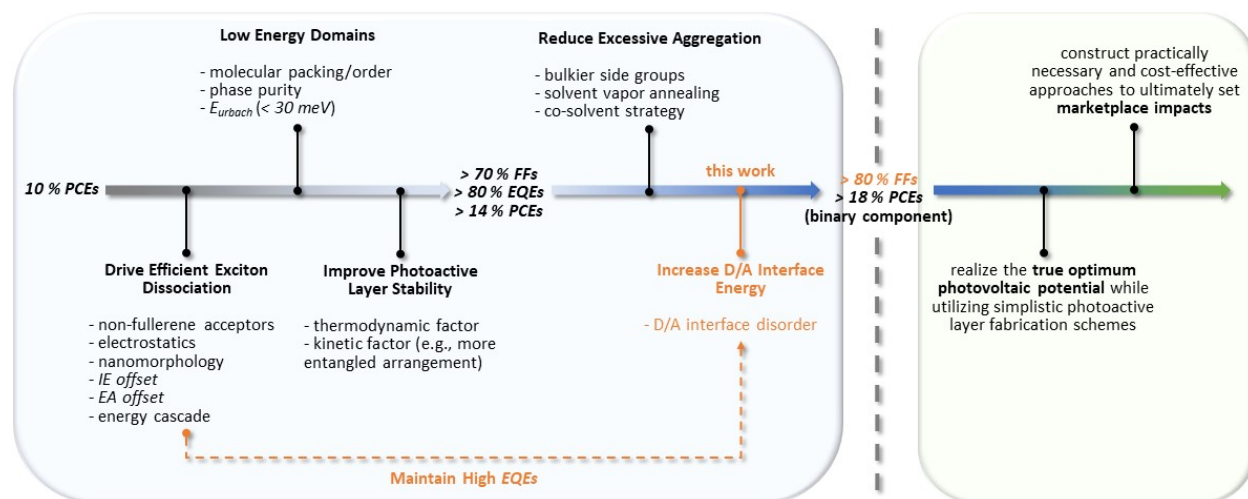
Fig. S20. A non-exhaustive and simplified framework of the strategies previously introduced to improve the commercial merits of OSCs based on efficiency and stability (more details are provided in the introduction) including the contribution and application of this work (orange-colored texts).

Supplementary Tables and Discussion

Table S1. Summary of photovoltaic performance under 1 Sun illumination

PM1:NFA	*PCE* (%)	*FF* (%)	V_{OC} (V)	J_{SC} (mA cm^{-2})
BTP-4F **(Y6)**	16.96 [16.51 ± 0.2]	74.87 [73.94 ± 0.5]	0.87 [0.86 ± 0.01]	26.33 [25.75 ± 0.3]
BTP-4F-**PC6**	18.39 [17.76 ± 0.4]	80.17 [79.12 ± 0.6]	0.87 [0.86 ± 0.01]	26.83 [25.97 ± 0.5]
BTP-4F-**P2EH**	17.71 [17.17 ± 0.2]	79.09 [78.44 ± 0.4]	0.89 [0.88 ± 0.01]	25.22 [24.82 ± 0.3]

PTQ10:NFA	*PCE* (%)	*FF* (%)	V_{OC} (V)	J_{SC} (mA cm^{-2})
BTP-4F **(Y6)**	16.43 [16.18 ± 0.2]	74.76 [73.66 ± 0.7]	0.87 [0.86 ± 0.01]	26.12 [25.53 ± 0.5]
BTP-4F-**PC6**	18.31 [17.93 ± 0.2]	80.82 [79.87]	0.88 [0.88 ± 0.01]	26.02 [25.53 ± 0.2]
BTP-4F-**P2EH**	17.04 [16.77 ± 0.2]	78.43 [77.86]	0.88 [0.88 ± 0.01]	24.98 [24.47 ± 0.3]

This table summarizes the obtained maximum photovoltaic performance under continuous 1 Sun illumination in an inert atmosphere, inside the square brackets are the corresponding average value and standard error. The statistics are obtained from at least 20 independent working solar cells for each system.

Discussion: It is apparent that the differences in *PCEs* are only evident from *FF* values. Although the P2EH-based device exhibits a slight increase in V_{OC}, this is compensated by the commonly observed trade-off with J_{SC}. These J_{SC} values agree with those calculated from integrated EQE (Fig. S4). The slight change in V_{OC} can be a consequence of a slightly higher P2EH bandgap (Table S3). Thus, the only parameter that substantially reflects the trend in *PCEs* is *FF*. Take note that the EQE and absorption spectra for P2EH display the largest blueshift followed by PC6, suggestive of less aggregation behavior than Y6. However, it cannot justify the *FF* variations. Smaller

aggregates increase the D/A interface area, which may induce negative impacts on the free charge recombination upon a certain threshold, thus lowering the *FFs*. On the other hand, it can promote more efficient charge dissociation. For the case of this study, *FFs* are enhanced while charge dissociation is barely influenced, probably because Y6 charge transfer process is already very efficient. Additionally, when the donor polymer is changed to PTQ10, the same relative device metrics as those obtained from the PM1 donor can be observed.

Table S2. Summary of the current-voltage characteristics extended analysis

PM1:NFA	G_{max} (m^{-3} s^{-1} / 10^{28})	P_{diss} (%)	P_{coll} (%)
BTP-4F **(Y6)**	1.65 ± 0.03	97.51 ± 2	88.36 ± 1
BTP-4F-**PC6**	1.64 ± 0.03	98.35 ± 2	91.59 ± 1
BTP-4F-**P2EH**	1.62 ± 0.01	96.13 ± 2	90.26 ± 1

This table summarizes the extended analysis of the *JV* curve characteristics which also reflect the relative photovoltaic performance of the devices considered. Herein, G_{max} is the maximum exciton generation rate, P_{diss} is the probability of charge dissociation at short-circuit (SC) conditions, and P_{coll} is the probability of charge collection at maximum power point (MPP). A more detailed explanation and calculation methodology are available elsewhere.[7]

Discussion: At SC, photogenerated free charges from exciton dissociation will be swept toward the electrodes by the built-in electric field. The free charge transport is very efficient under this condition such that the influence of energetic defects/traps and other obstacles for charge transport and collection are minimal. Thus, the dissociation of excitons (i.e., neutrally charged) will dominantly impact P_{diss}. On the contrary, at MPP, the built-in electric field is already almost completely vanished by the externally applied bias, leading to less efficient free charge transport and collection.

The P2EH-based device exhibits marginally lower G_{max}, this can be attributed to the slight blueshift in its absorption and optical gap (Fig. S1). On the other hand, the charge dissociation is comparably efficient for all systems while both PC6 and P2EH-based devices display an apparent improvement for charge transport/collection, as suggested from the value of P_{coll}.

Table S3. Bandgap estimations and Urbach energy

NFA	E_g^{PV} (eV)	E_{opt} (eV)	E_{Urbach} (meV)
BTP-4F **(Y6)**	1.42	1.44	25
BTP-4F-**PC6**	1.42	1.45	24.53
BTP-4F-**P2EH**	1.43	1.47	25.09

Discussion: The photovoltaic bandgaps (E_g^{PV}) are calculated from the sensitivity measured EQE (sEQE) spectra of blends using the equation shown below. The probability density $P(E)$ is defined as $dEQE/dE$ (Fig. S2) and the limits of integration can be arbitrarily chosen, herein they correspond to the 50% probability points. This bandgap is a property of a fully operational (i.e., complete) device, a more detailed discussion concerning these properties is available in earlier works.[7] On the other hand, the more commonly reported optical bandgap (E_{opt}) is based on thin films which is generally estimated from the intersection of absorption and Jacobian-corrected photoluminescence (PL) spectra.

$$E_g^{PV} = \frac{\int E\,P(E)\,dE}{\int P(E)\,dE}$$

The Urbach energies (E_{Urbach}) are obtained by exponential fitting of sEQE spectra in the onset region (Fig. S8). It must be noted that the absorption coefficient (α) is proportional to EQE. From the inset of Fig. 2a, it is illustrated that the absorption exponential tail consists of contributions from the D/A interface (or CTS) and acceptor-rich domains, as observed from several studies in fullerene-based systems.[8] Although it is usually not the same case for NFA-based systems owing to low CTS absorption cross-section that largely overlaps with the acceptor absorption edge. To the best of our knowledge, sEQE is by far one of the most sensitive and commonly used technique to fit the absorption onset features as compared to standard UV-Vis-NIR absorption setups. Values of E_{Urbach} comparable to ambient thermal energy (i.e., 25 meV) suggest that energetically trapped charge carriers can be thermally de-trapped, potentially enhancing charge transport and mobilities.

$$\alpha = \alpha_0\,exp\left(\frac{E}{E_{Urbach}}\right)$$

Surprisingly, there are no apparent differences in the E_{Urbach} for all the systems considered even after the burn-in degradation (Fig. S8) despite photovoltaic measurements indicate that charge recombination increased after the burn-in. It is indisputable that E_{Urbach} is an essential parameter to mitigate charge recombination, as cited by several reports, but it is not sufficient to explicitly clarify how remarkable *FFs* (i.e., > 80 %) can be achieved nor the burn-in efficiency loss mechanisms.

Table S4. Urbach energies from earlier literatures

Blend	E_{Urbach} (meV)	PCE (%)	FF (%)	Year Published
PBDB-T-2F:ITIC[9]	25	7.9	61	2017
J71:ITIC[9]	27	8.4	65	2017
PCPDTBT:PCBM[9]	48	4.4	52	2018
PBDB-T:IEICO-4F[9]	24	7.3	62	2018
PTB7-Th:PC$_{71}$BM[10]	45.02	7.40	61	2019
PTB7-Th:ITIC[10]	54.44	6.84	60	2019
PTB7-Th:1PDI-ZnP[11]	49.1	3.10	36.2	2019
PTB7-Th:2PDI-ZnP[11]	42.7	5.33	51.4	2019
PTB7-Th:4PDI-ZnP[11]	38.1	8.35	64	2019
PM6:BZ4F-5[11]	31.2	12.86	69.58	2019
PM6:BZ4F-6[11]	25.6	15.14	73.51	2019
PM6:BZ4F-7[11]	22.9	16.17	75.21	2019
PBDB-T-2F:IT-4F[9]	27	11.1	74	2019
PBDB-T-2F:Y7[9]	26	14.1	71	2019
J71:IT-4F[9]	30	9.1	58	2019
PM6:Y11[11]	25.6	16.54	74.33	2020
PM6: PC$_{71}$BM[11]	46.5	9.06	72.30	2020
D16:Y6Se[12]	20.4	17.7	75.3	2020
PTB7:PCBM[9]	57	7.8	70	2020
D18:Y6[13]	25.23	16.8	74.4	2021
D18:BTPR:Y6[13]	24.85	17.5	74.6	2021
PM6:DRTB-T-C4:Y6[14]	23.6	17.05	80.88	2021
PM6:CNS-6-8:Y6:PC$_{71}$BM[15]	23.44	17.80	77.8	2022
PM6:Y6:PC$_{71}$BM[15]	24.39	16.83	75.6	2022
ZR-C8:Y6[16]	25.38	11.8	58.3	2022
ZR-SiO:Y6[16]	23.44	15.8	71.4	2022
ZR-SiO-EH:Y6[16]	22.90	16.1	73.3	2022
TB-F:L8-BO[17]	24.8	16.7	76.7	2022
BTR-Cl:L8-BO[17]	26.2	14.7	73	2022
TB:L8-BO[17]	26	15.6	74.2	2022
PM6:PY-V-γ[18]	22	16.9	75.5	2022
PM6:PY-T-γ[18]	23.9	15.8	71.5	2022
PM6:PY-2T-γ[18]	24	15	69.5	2022
PM1:**Y6**	25	16.51	73.94	**this study**

PM1:BTP-4F-**PC6**	24.53	17.76	79.12	**this study**
PM1:BTP-4F-**P2EH**	25.09	17.17	78.44	**this study**

Discussion: Since the evolution of NFA-based systems, the spectral features distinguishing CTS and NFA-domains in EQE exponential tails are no longer clearly noticeable through most measurement sensitivity limits. Herein, such exponential fittings are sought to mainly correspond to the characteristics of purer domains which then dominate literature reports. As illustrated in Fig. 2b and Table S4, by considering a wide range of single-junction OSCs (binary and ternary), it is clear that *PCEs* and *FFs* are highly influenced by E_{Urbach}, consistent with several former observations. However, by explicitly considering current state-of-the-art systems and their recent predecessors (i.e., defined here to display > 15 % *PCEs*), it is very challenging to realize any concrete correlations. It must also be noted that exponential fittings to obtain E_{Urbach} are influenced by the selected fitting range (in addition to other factors) wherein a deviation of at least ±1 meV can be roughly estimated, thus many of the recent arguments and claims remain impartial. Empirically, E_{Urbach} less than 30 meV is customarily for most OSCs with *PCEs* > 14 %. Further, due to the influence of thermal broadening, E_{Urbach} is limited in the neighborhood of around 25 meV under ambient conditions. Consequently, E_{Urbach} is not sufficient to understand the mechanism explaining how the limited number of current state-of-the-art OSCs can reach remarkable *FFs* and *PCEs*.

Table S5. Singlet exciton dissociation and charge transfer

Blend	*Fluence (μJ cm^{-2})*	τ_{fast} *(ps)*	τ_{slow} *(ps)*
PM1:Y6	3.18	0.75 ± 0.06	10.69 ± 0.67
	9.55	0.49 ± 0.03	4.90 ± 0.29
PM1:PC6	3.18	1.74 ± 0.08	16.63 ± 0.54
	9.55	1.13 ± 0.05	11.84 ± 0.40
PM1:P2EH	3.18	1.71 ± 0.13	14.31 ± 0.36
	9.55	1.33 ± 0.07	9.33 ± 0.33
after burn-in			
PM1:P2EH	3.18	1.26 ± 0.08	14.10 ± 0.60
	9.55	1.03 ± 0.07	$6.62 \quad \pm 0.32$

Table S6. Polaron recombination kinetics

Blend	*Fluence (μJ cm^{-2})*	τ_{D+} *[τ_{A-}] (ns)*	τ_{ave} *(ns)*
PM1:Y6	9.55	0.95 ± 0.08 $[1.30 \pm 0.14]$	1.13 ± 0.11
PM1:PC6	9.55	1.20 ± 0.11 $[1.49 \pm 0.13]$	1.35 ± 0.12
PM1:P2EH	9.55	1.15 ± 0.06 $[1.46 \pm 0.07]$	1.31 ± 0.07
after burn-in			
PM1:P2EH	9.55	0.95 ± 0.05 $[1.42 \pm 0.09]$	1.19 ± 0.07

Supplementary Notes

Note S1. Order-disorder phase transitions from photoluminescence

The photoluminescence (PL) of neat NFAs and their blend with PM1 are shown in Fig. 1c. It can be noticed that the PL spectra of neat NFAs are not perfectly symmetric, suggesting contributions from distinct phases with different disorder.[19] Hence, the PL spectra are deconvoluted herein using Gaussian functions. For all the neat NFAs, two Gaussians centered at C1 (lower wavelength) and C2 (higher wavelength) were able to replicate the PL lineshape. Interestingly, the C1 contribution becomes more apparent in PC6 and P2EH. By recalling their solid-state characteristics, the more apparent C1 can then be understood as a consequence of the reduced aggregation for PC6 and P2EH thereby increasing the aggregate-aggregate interface area (i.e., more randomly oriented). This is consistent with previous reports demonstrating that the higher energy peak will be more evident upon increasing the disorder.[19] Consequently, the Gaussian centered at C1 are assigned for the disordered phase (i.e, aggregate-aggregate interfaces) while those centered at C2 is for the NFAs self-assembly. The Gaussian at C1 may not be relevant in understanding their photovoltaic performance since the D/A interface will dominate in the actual blend. On the other hand, C2 will depend on the aggregation behavior and the nature of interacting chromophores in the NFA self-assemblies.[19] Nevertheless, it was found from Urbach tails and GIWAXS that all the NFAs considered herein self-assemble into a highly ordered fashion with crystalline characteristics. Furthermore, it is also possible that other vibrionic peaks will convolute with the C2 Gaussian. However, vibrational progressions alone cannot explain why the C1/C2 ratio substantially increases from Y6 to PC6 to P2EH. On the other hand, the increasing fraction of aggregate-aggregate interfaces in the bulk owing to significantly reduced domain size in PC6 and P2EH justified the C1/C2 ratio. Hence, it is suggestive that the assigned C1 and C2 are dominantly influenced by the relative disorder of different phases present in the bulk.

By turning into the PL of blends, blue shifted peaks can be observed relative to neat NFAs Gaussian at C2. In order words, it suggests an uphill energy transition from NFA-rich domains to D/A interfaces. The most pronounced shift is observed from the P2EH-based blend. To further substantiate the mentioned transport energy landscape, the diffusion-limited exciton dissociation

and CTS kinetics which involve the charge carrier transport from NFA-rich domains to D/A interfaces are also investigated. Meanwhile, the PL intensity quenching (PL_Q) of blends relative to neat NFAs is descriptive of hole transfer efficiency (i.e., from NFA to PM1). Devices based on P2EH demonstrate a slightly lower PL_Q which supports the EQE and suggests less efficient NFA exciton dissociation.

Note S2. Electroabsorption spectroscopy

Electroabsorption (EA) is based on the shift in absorption due to the presence of an electric field modulating the electron density distribution of molecular orbitals, this is known as the Stark effect. In OSCs, generating free electrons and holes upon exciton dissociation will lead to induced dipoles and electric field, causing the Stark effect. Thus, EA features are also commonly used to understand charge transfer processes. In this study, the EA ($\Delta R/R$) spectra of devices consisting of donor and acceptor blends are obtained via reflectance geometry measurements at a bias of -2 V and amplitude of peak-peak voltage of 4 V of a sine electric field, R is the reflection intensity. It is also shown in Fig. S6-3 that varying the bias and amplitude voltage will not significantly influence the EA lineshapes. Negative bias is applied to minimize the current injection during the EA measurements.

The EA at 1st and 2nd harmonics of the modulating frequency of the electric field were measured (see Methods for the details) and deviations in their lineshapes can be associated with non-isotropic permanent dipole moments in the molecule. These permanent dipoles can only influence the lineshapes of the 1st harmonic since the quadratic Stark effect entirely governs the 2nd harmonic, a more detailed discussion is available elsewhere.[20] As shown in Fig. S6-2, more pronounced deviations in the 900-1000 nm range can be observed for PM1:PC6 and PM1:P2EH devices than PM1:Y6. Further, additional significant dipole contributions can be inferred in the range 650-750 nm (both for PM1:PC6 and PM1:P2EH) and 580-620 nm (for PM1:PC6). Hence, inductive effects from the substitution of alkyl side chains with 2D phenylalkyl side groups can appreciably induce permanent dipole moments in the NFAs. Consequently, there will be an increase in the average electrostatic potentials (ESP) and thereby enhancing the electron withdrawing property of the NFAs.[21,22] This is known to be beneficial for charge transfer and dissociation.[21] Additionally, the solubility in polar organic solvents (e.g., chloroform and chlorobenzene) can be enhanced which influences the solid-state assembly.[23,24]

Note S3. Electroluminescence spectroscopy

Electroluminescence (EL) spectroscopy has been an extremely valuable technique for understanding intermolecular charge transfer states (CTS) in OSCs. It operates by injecting electrons/holes into the OSC device which bimolecularly recombines, acting similarly to light emitting diodes (LED). Interestingly, an emission distinctly different than the emission of the donor and acceptor components have been previously observed, suggestive of an additional quantum state.[25-27] This state is understood as the CTS existing through the molecular interface formed by the donor and acceptor molecules.[28] Further, several studies concluded that such interfaces are the origin (or at least the dominant precursor) of photogenerated free charges (i.e., electron and hole polarons).[29] For quantitative values corresponding to the property of CTS, the reduced EL (*rEL*) can be fitted through Gaussian functions based on the Marcus theory of electron transfer. A more detailed explanation and quantum-mechanical derivation can be found elsewhere.[25]

$$rEL = \frac{f}{\sqrt{4\pi\lambda_{RO}\Phi_T}}exp\left(\frac{-\left(E_{CTS}-\lambda_{RO}-E\right)^2}{4\lambda_{RO}\Phi_T}\right)$$

Here, *rEL* is *EL/E* where E is the photon energy (eV), f is a pre-exponential factor, λ_{RO} is CTS reorganization energy (eV), Φ_T is thermal energy (eV), and E_{CTS} is the CTS energy (eV). It must be noted that further division of *rEL* by E^2 is typically necessary for Jacobian correction,[30] depending on the type of spectrometer used. It is also worthy to deconvolute the blend EL spectra and disentangle contributions from CTS and acceptor singlets.[31] Hence, spectra are fitted with two or three Gaussians, depending on the relative fitting coefficients, while the Gaussian with the lowest energy is assigned to CTS.

As seen in Fig. S5, simulations showed that larger λ_{RO} would cause broader and redshifted CTS emissions. However, there is an insignificant effect of increasing temperature beyond ambient conditions (300 K) up to certain values that are practically reachable upon continuous 1 Sun illumination. Former studies in fullerene-based systems which can clearly distinguish the absorption exponential tail features and specific energetic disorder corresponding to D/A interface and NFA-domains found that this λ_{RO} is a direct measure of D/A interface disorder.[8] Consequently, λ_{RO} is a useful metric to understand the relative energetic disorder of such molecular interfaces.

The D/A interface energy referred to in this work may not be directly equivalent to E_{CTS}. Such interface energy is established from HOMO/LUMO of disordered and ordered phases of the molecules which translates to transport energy levels associated with mobile free charges. On the other hand, the E_{CTS} is based on energy levels prior to recombination wherein internal relaxations and other energy exchanges have occurred thereby not directly representing mobile charges. Nevertheless, the E_{CTS} values remain a convenient initial indication of relative D/A interface energy.

Note S4. Understanding the transient absorption spectral features

Upon considering the visible detection range (450 – 800 nm), the selective excitation of PM1 displays positive features at 500 - 650 nm while negative features at 660 - 800 nm, as shown in Fig. S14-1(a,b). Since the positive features are around the PM1 absorption range and there is no apparent spectral shape variation with delay time, it can be assigned to PM1 ground state bleach (GSB). After photon absorption, the ground state will be de-occupied until replenished by charge recombination and internal conversions. Thus, there will be a negative change in absorption (ΔA) or equivalently positive change in transmission ($\Delta T/T$), defined as GSB.

To understand the negative features, the PM1:PCBM blend is also measured. Fortunately, it has been widely reported that PCBM transient absorption signals in this range are negligible. It must be noted that neat PM1 thin film will mostly generate PM1 singlets (PM1*) upon excitation and only few populations can undergo charge dissociation forming PM1 hole polarons (PM1$^+$). On the other hand, by blending with the acceptor PCBM, the population of PM1$^+$ will be more pronounced. Evidently from Fig. S14-2(a), the broad negative features appear deeper when blended with PCBM, this can be attributed to greater photo-induced absorption (PIA) from the increasing PM1$^+$ population. Also, it is clear that early after excitation there is a very deep negative features around 680 - 720 nm for the PM1:PCBM blend which matches the PM1 EA as per its absorption is located. Further discussion about EA is provided in Supplementary Notes. Fluence-dependence is performed to further confirm that PM1$^+$ PIA contributes to the negative features at 680 – 800 nm, as shown in Fig. S14-2(b). At higher excitation fluence, there will be higher energy to increase the probability of PM1 singlet dissociation in neat PM1, leading to larger PM1$^+$ population and more intense PIA. It must be noted that from the PL spectra, PM1* stimulated emissions (SE) are expected to overlap in the 640 - 800 nm range.

By turning into PM1 GSB dynamics in neat PM1 (Fig. S14-2(c)), two distinctly different decay lifetimes are obtained. The shorter lifetime (3 ps) matches the rise time of the PM1 EA (700 nm), indicating singlet dissociation forming PM1$^+$. The longer lifetime (49 ps) can then be attributed to the decay of PM1 singlet excitons which does not have fluence dependence up to 5.1 μJ cm^{-2} (Fig. S14-2(d)).

For the actual blend, the electron transfer kinetics (i.e., from PM1 to NFA) can be understood from the PM1 singlet GSB decay in early time scales which will be followed by the rising PM1$^+$ polaron

GSB in the same wavelength range. The polarons located at the donor/acceptor will give rise to similar GSB as with the corresponding singlets but lack SE as they are non-emissive. As shown in Fig. S14-3(b), such electron transfer (in combination with energy transfer) is suggestive to be ultrafast and cannot be probed by our setup owing to the instrument response limit. This is already expected based on several reports in other high-performing polymer donors and justifying the almost completely quenched donor exciton PL in blends. Hence, the 400 nm excitation of PM1:Y6 will give rise to much longer presence of the 550 - 650 nm GSB features due to $PM1^+$, as shown in Fig. S14-3(a). To support this, the Y6 can be selectively excited in the blend using an 800 nm pump. After Y6 singlet dissociation, there will be hole transfer to the polymer donor PM1, giving rise to $PM1^+$ population. Indeed, even at 0.5 ps after Y6 excitation, the $PM1^+$ GSB is already evident (Fig. S14-3(b)), suggesting a fast hole transfer component from Y6 to PM1. After 15 ps, the Y6 singlet GSB is already substantially diminished suggesting that most singlets have already dissociated. However, the GSB at 550 - 650 nm remains and is longer-lived, implying that this feature comes from $PM1^+$.

Additionally, in Fig. S14-3(b), the $PM1^+$ GSB features at 500 - 600 nm become more in-shape at time scales wherein most of the NFA singlets have decayed. This is due to the characteristic absorption of the considered NFA singlets causing PIA-like features that drags portions of the $PM1^+$ GSB in early time scales (<1 ps) and decays analogous to the NFA singlet GSB. Consequently, the $PM1^+$ GSB peak position is monitored only after 5 ps wherein the signals are already largely dominated by polarons thereby can provide more meaningful information about their energy transition upon migration to purer domains at longer time scales.

The NIR detection range (820 nm - 1200 nm) is used here to probe the PIA of NFA electron polarons (NFA^-). The NFA singlet excitons are found to live only up to less than 0.5 ns but the polaron PIA remains even at 7 ns (Fig. S15-1). Similar with previous reports for Y6 blends,[3] it is clearly observable that only the blends exhibit recognizable NFA^- PIA when compared to pure acceptors as a consequence of exciton dissociation (Fig. S15-2). The PIA features at 1050 nm - 1150 nm are then almost exclusive to electron polarons. It must also be noted that the tail of hole polarons PIA (Fig. S15-3) is also visible on the same range. But, since the peak of hole polarons is closer to 900 nm (overlapping with shorter-lived NFA singlet PIA) while the observed polaron peak is closer to 1000 nm, then it is suggestive that the detection from $1050 - 1150$ nm is dominated

by NFA electron polarons. Nevertheless, both hole and electron polarons define the charge generation and recombination behavior. These assignments have previously been elaborated with great detail by Ohkita et al. wherein the NFA⁻ PIA rise time is shown to effectively represent the exciton dissociation forming electron and hole polarons while its decay reflects the charge recombination.[3]

Note S5. Exciton dissociation and charge recombination

Singlet exciton dissociation strongly influences the EQE and consequently the device J_{SC}. In addition, the material bandgap and absorption range are also major factors in expanding the photon harvesting ability, ultimately reflecting the photocurrent generation. It can be observed that P2EH absorption in solid-state has a slight hypsochromic shift relative to Y6 and PC6 which is believed to contribute for its modestly lower J_{SC}. Another thing that can influence the J_{SC} is the reduced EQE for P2EH-based device which can be an indication of less efficient exciton dissociation. Both diffusion-limited and upfront dissociation can significantly manifest free charge generation. The higher energy difference between the D/A interface and purer domains is sought to increase the total energy requirement for diffusion-limited dissociation as charge carriers must move from lower energy to higher energy positions, this can potentially increase the geminate recombination losses. Nevertheless, most high efficiency polymers and Y-series NFAs display very efficient exciton dissociation through the contribution of several factors such as thermal energy, energy offsets, nanomorphology, electrostatic effects, and intramolecular interactions (just to name a few). Consequently, their properties enable them to have a relatively high tolerance with such D/A interfacial energy effect. For instance, even though P2EH-based blend have higher interface energy than Y6, its EQE remains high (> 80 %). Likewise, in addition to the enhanced electrostatic effects owing to the larger average permanent dipole moment, the reduced aggregation of PC6 and P2EH are also sought to aid the exciton dissociation.

Now turning into the advantages of higher D/A interface energy, the upfront exciton dissociation will be favored owing to downhill energy cascade configurations.[3] However, when comparing Y6, PC6, and P2EH-based blends having near perfect exciton dissociation, such merits could be insignificant. On the other hand, it will also elevate the energy requirement for free charges to recombine through D/A interfaces, this is found to remarkably improve charge transport reflecting high *FFs*. Meanwhile, because PC6 has stronger solid-state aggregation behavior than P2EH, which is also known to be beneficial for charge transport, it displays marginally higher *FF* than those of P2EH-based devices. There are number of reports in high efficiency OSCs citing bimolecular origin as the primary cause of recombination losses,[32] consequently it is not surprising to observe such notable *FFs* when the D/A interface energy is properly designed. By taking

advantage of this important principle, both PC6 and P2EH-based devices can achieve *FFs* of over 80 %.

Aside from the interface-tuning strategy based on NFA outer side chain modification adopted in this work, there could be other methods from molecular designs to device engineering and their combinations suitable for commercial adaptations. However, the property-functionality interplay of D/A interfaces presented in this work will serve as a fundamental principle to effectively screen and direct potential approaches.

Methods

Materials availability. PM1 and Y6 are commercially available from Solarmer Inc., whose lot No. are YM421A and KKC10A. PC6 and P2EH are independently synthesized in the laboratory according to the reported methods [Energy Environ. Sci. 2021, 14, 3469.; Adv. Energy Mater. 2021, 11, 2102596.].

Device fabrication. Solar cells were fabricated in a conventional configuration of ITO/PEDOT:PSS/active layers/PFN-Br-MA/Ag. The ITO substrates were first scrubbed by detergent and then sonicated with deionized water, acetone and isopropanol subsequently, and dried overnight in an oven. The glass substrates were treated by UV-Ozone for 30 min before use. PEDOT:PSS (Al4083 from Hareus) was spin-cast onto the ITO substrates at 7500 rpm for 30 s, and then dried at 160 °C for 15 min in ambient atmosphere. The PM1:NFAs blends (weight ratios 1:1.2 for all) were dissolved in chloroform (the concentration of donor was 7 mg mL-1), with 1-chloronaphthalene (0.7% vol) as additive, and stirred at 50 °C hotplate for 2 hours. The blend solution was spin-cast at 2000-2500 rpm for 30 s onto PEDOT:PSS film followed by a temperature annealing of 100°C for 1 min. A thin PFN-Br-MA layer (0.5 mg/mL in methanol and 0.25% wt% melamine, 3000 rpm) was coated on the active layer, followed by the deposition of Ag (evaporated under 3×10-4 Pa through a shadow mask). The optimal active layer thickness measured by a Bruker Dektak XT stylus profilometer was about 110 nm.

Solar simulation. The current density-voltage (J-V) curves of devices were measured using a Keysight B2901A Source Meter in glove box under AM 1.5G (100 mW cm-2) using an Enlitech solar simulator. The device contact area was 0.042 cm2, device illuminated area during testing was 0.0324 cm2, which was determined by a mask. A step voltage of 0.1 – 0.5 V with about 5 ms delay time are used. Device measurements and thermal ageing were conducted inside the glovebox under an inert atmosphere.

SCLC mobilities. The electron and hole mobilities were measured by using the method of space-charge limited current (SCLC) for electron-only devices with the structure of ITO/ZnO/active layer/PFN-Br-MA/Ag.

Absorption and photoluminescence spectroscopy. The steady-state absorption measurements were conducted using UV-Vis-NIR spectrophotometer Lambda 950 from Perkin Elmer while PL spectra were collected using InVia (Renishaw) spectrometer with sample excitation at 632.8 nm laser.

External quantum efficiency. The EQE spectra were measured using a Solar Cell Spectral Response Measurement System QE-R3011 (Enlitech Co., Ltd.). The light intensity at each wavelength was calibrated using a standard monocrystalline Si photovoltaic cell.

Sensitively measured external quantum efficiency. The sEQE spectra of devices were collected at short-circuit conditions using monochromatic illumination from a combination of a monochromator and 150 W tungsten lamp. An optical chopper modulated the light beam with a frequency of 405 Hz, and the device photocurrent was measured as a function of the incident photon energy (wavelength) using a lock-in amplifier (Stanford Instrument SR 850), and the incident light power was measured with a power meter (Newport 918D-UV-0D3R).

Electroabsorption spectroscopy. The electroabsorption spectrum was measured with the device structure. The beam of 150 W tungsten lamp went through a monochromator and was focused on the sample area covered by the Ag electrode. The reflected light intensity, R, was detected by the Si photodetector. Meanwhile, A sine wave electric field was applied to the electrodes of testing devices. The changes in reflection, ΔR, was detected by the Si photodetector connected to a lock-in Amplifier under the first and second harmonic frequency of modulating field. The EA intensity was calculated as ΔR/R.

Ultraviolet photoelectron spectroscopy. UPS measurements were done using Kratos Axis Ultra DLD multitechnique surface analysis system (Axis Ultra DLD) with He(I) (21.22eV) energy source and using a step resolution of 25 meV. A 5 V bias was applied during the measurements.

Transient absorption spectroscopy. Near-infrared (850-1600 nm) femtosecond transient absorption spectroscopy was performed using an apparatus previously described.[33] Briefly, 50% of the output of a 1 kHz, 1W, 100 fs Ti:sapphire laser system with a 827 nm fundamental (Tsunami oscillator/Spitfire amplifier, Spectra-Physics LLC) was used to pump a commercial collinear optical parametric amplifier (TOPAS-Prime, Light-Conversion LLC) tuned to 800. The pump was depolarized to suppress effects due to polarization-dependent dynamics and attenuated to the

specific energy density. The pump was focused to a 1 mm diameter spot at the sample position. The probe was generated using 10% of the remaining output to drive continuum generation in a proprietary crystal and detected on a commercial spectrometer (customized Helios, Ultrafast Systems LLC). The films were measured at room temperature under a vacuum of 10-3 torr to minimize potential sample degradation due to air exposure. A similar setup is used for the visible probe (450 – 800 nm), as previously described.[34]

Time-resolved photoluminescence. The sample was excited with a Ti:sapphire oscillator at 805 nm with a repetition rate of 76 MHz. The time resolved photoluminescence at 850-860 nm was collected and detected by a streak camera (Hamamatsu).

Device capacitance. E4980A Precision LCR Meter was used to measure the capacitance-voltage characteristic of each cells at under dark. The high terminal was connected to the 1kHz common anode. The low terminal was connected to the cathode of the target cell. The low terminal was chosen to be connected with the smallest area of interest because the ammeter is fixed at low terminal side of the machine such that the configuration can minimize the interference from cells.

Density functional theory simulations. The calculation of geometry optimization was performed by the Gaussian 16 program[35] using the B3LYP-D3/6-311(d, p) with dispersion corrections.[36,37] The dipole moment was calculated using the B3LYP-D3/def2-TZVPD containing the diffuse basis to obtain accurate values.[38] The Multiwfn program was used for result visualization. The calculations are carried out on molecules with full-side chains.

References

1   Zhang, J. *et al.* Alkyl-Chain Branching of Non-Fullerene Acceptors Flanking Conjugated Side Groups toward Highly Efficient Organic Solar Cells. *Advanced Energy Materials* **11**, 2102596 (2021).

2   Ouyang, J., Wu, F., Zhao, X. & Yang, X. Regulating the Crystallinity and Self-Aggregation of Fused Ring Electron Acceptors via Branched Side-Chain Engineering for Efficient Organic Solar Cells. *Small*, 2201769 (2022).

3   Natsuda, S.-i. *et al.* Cascaded energy landscape as a key driver for slow yet efficient charge separation with small energy offset in organic solar cells. *Energy & Environmental Science* **15**, 1545-1555 (2022).

4   Gao, W. *et al.* Regulating exciton bonding energy and bulk heterojunction morphology in organic solar cells via methyl-functionalized non-fullerene acceptors. *Journal of Materials Chemistry A* **7**, 6809-6817 (2019).

5   Karuthedath, S. *et al.* Intrinsic efficiency limits in low-bandgap non-fullerene acceptor organic solar cells. *Nature Materials* **20**, 378-384 (2021).

6   Schwarze, M. *et al.* Impact of molecular quadrupole moments on the energy levels at organic heterojunctions. *Nature communications* **10**, 1-9 (2019).

7   Dela Peña, T. A. *et al.* Understanding the Charge Transfer State and Energy Loss Trade-offs in Non-fullerene-Based Organic Solar Cells. *ACS Energy Letters* **6**, 3408-3416 (2021).

8   Jain, N. *et al.* Interfacial disorder in efficient polymer solar cells: the impact of donor molecular structure and solvent additives. *Journal of Materials Chemistry A* **5**, 24749-24757 (2017).

9   Jain, N. *et al.* Role of Electronic States and Their Coupling on Radiative Losses of Open-Circuit Voltage in Organic Photovoltaics. *ACS Applied Materials & Interfaces* **13**, 60279-60287 (2021).

10   Duan, L. *et al.* Comparative study of light-and thermal-induced degradation for both fullerene and non-fullerene-based organic solar cells. *Sustainable energy & fuels* **3**, 723-735 (2019).

11   Yuan, J. *et al.* Effects of energetic disorder in bulk heterojunction organic solar cells. *Energy & Environmental Science* **15**, 2806-2818 (2022).

12   Zhang, Z. *et al.* Selenium heterocyclic electron acceptor with small urbach energy for as-cast high-performance organic solar cells. *Journal of the American Chemical Society* **142**, 18741-18745 (2020).

13   Zhang, Y. *et al.* An electron acceptor analogue for lowering trap density in organic solar cells. *Advanced Materials* **33**, 2008134 (2021).

14   Zeng, Y. *et al.* Exploring the charge dynamics and energy loss in ternary organic solar cells with a fill factor exceeding 80%. *Advanced Energy Materials* **11**, 2101338 (2021).

15   Feng, W. *et al.* Tuning Morphology of Active Layer by using a Wide Bandgap Oligomer-Like Donor Enables Organic Solar Cells with Over 18% Efficiency. *Advanced Energy Materials* **12**, 2104060 (2022).

16   Chang, Y. *et al.* Regulating phase separation and molecular stacking by introducing siloxane to small-molecule donors enables high efficiency all-small-molecule organic solar cells. *Energy & Environmental Science* (2022).

17   Li, Z. *et al.* Over 17% efficiency all-small-molecule organic solar cells based on an organic molecular donor employing 2D side chain symmetric-breaking strategy. *Energy & Environmental Science* (2022).

18   Yu, H. *et al.* A Vinylene-Linker-Based Polymer Acceptor Featuring Co-planar and Rigid Molecular Conformation Enables High-Performance All-Polymer Solar Cells. *Advanced Materials*, 2200361 (2022).

19   Kroh, D. *et al.* Identifying the Signatures of Intermolecular Interactions in Blends of PM6 with Y6 and N4 Using Absorption Spectroscopy. *Advanced Functional Materials*, 2205711 (2022).

20   Siebert-Henze, E. *et al.* Built-in voltage of organic bulk heterojuction pin solar cells measured by electroabsorption spectroscopy. *AIP Advances* **4**, 047134 (2014).

21   Li, J. *et al.* Influence of Large Steric Hinderance Substituent Position on Conformation and Charge Transfer Process for Non-Fused Ring Acceptors. *Small Methods* **6**, 2200007 (2022).

22   Xu, Y., Yao, H., Ma, L., Wang, J. & Hou, J. Efficient charge generation at low energy losses in organic solar cells: a key issues review. *Reports on Progress in Physics* **83**, 082601 (2020).

23   Ans, M., Ayub, K., Bhatti, I. A. & Iqbal, J. Designing indacenodithiophene based non-fullerene acceptors with a donor–acceptor combined bridge for organic solar cells. *RSC advances* **9**, 3605-3617 (2019).

24   Qiu, W. & Zheng, S. Designing and Screening High-Performance Non-Fullerene Acceptors: A Theoretical Exploration of Modified Y6. *Solar RRL* **5**, 2100023 (2021).

25   Vandewal, K., Tvingstedt, K., Gadisa, A., Inganäs, O. & Manca, J. V. Relating the open-circuit voltage to interface molecular properties of donor: acceptor bulk heterojunction solar cells. *Physical Review B* **81**, 125204 (2010).

26   Benduhn, J. *et al.* Intrinsic non-radiative voltage losses in fullerene-based organic solar cells. *Nature Energy* **2**, 1-6 (2017).

27   Coropceanu, V., Chen, X.-K., Wang, T., Zheng, Z. & Brédas, J.-L. Charge-transfer electronic states in organic solar cells. *Nature Reviews Materials* **4**, 689-707 (2019).

28   Tvingstedt, K. *et al.* Electroluminescence from charge transfer states in polymer solar cells. *Journal of the American Chemical Society* **131**, 11819-11824 (2009).

29   Deibel, C., Strobel, T. & Dyakonov, V. Role of the charge transfer state in organic donor–acceptor solar cells. *Advanced materials* **22**, 4097-4111 (2010).

30   Mooney, J. & Kambhampati, P. Vol. 4   3316-3318 (ACS Publications, 2013).

31   Eisner, F. D. *et al.* Hybridization of local exciton and charge-transfer states reduces nonradiative voltage losses in organic solar cells. *Journal of the American Chemical Society* **141**, 6362-6374 (2019).

32   Gillett, A. J. *et al.* The role of charge recombination to triplet excitons in organic solar cells. *Nature* **597**, 666-671 (2021).

33   Young, R. M. *et al.* Ultrafast conformational dynamics of electron transfer in exbox4+⊂ perylene. *The Journal of Physical Chemistry A* **117**, 12438-12448 (2013).

34   Wang, Z. *et al.* Insight into the Enhanced Charge Transport in Quasi-2D Perovskite via Fluorination of Ammonium Cations for Photovoltaic Applications. *ACS Applied Materials & Interfaces* **14**, 7917-7925 (2022).

35   Gaussian09, R. A. 1, mj frisch, gw trucks, hb schlegel, ge scuseria, ma robb, jr cheeseman, g. Scalmani, v. Barone, b. Mennucci, ga petersson et al., gaussian. *Inc., Wallingford CT* **121**, 150-166 (2009).

36   Goerigk, L. *et al.* A look at the density functional theory zoo with the advanced GMTKN55 database for general main group thermochemistry, kinetics and noncovalent interactions. *Physical Chemistry Chemical Physics* **19**, 32184-32215 (2017).

37   Grimme, S., Antony, J., Ehrlich, S. & Krieg, H. A consistent and accurate ab initio parametrization of density functional dispersion correction (DFT-D) for the 94 elements H-Pu. *The Journal of chemical physics* **132**, 154104 (2010).

38   Rappoport, D. & Furche, F. Property-optimized Gaussian basis sets for molecular response calculations. *The Journal of chemical physics* **133**, 134105 (2010).